

A CATALOG OF QUASAR PROPERTIES FROM SDSS DR7

YUE SHEN¹, PATRICK B. HALL², GORDON T. RICHARDS³, DONALD P. SCHNEIDER⁴, MICHAEL A. STRAUSS⁵

Draft version May 20, 2010

ABSTRACT

We present a compilation of properties for the 105,783 quasars in the SDSS Data Release 7 (DR7) quasar catalog. In this value-added product, we compile continuum and emission line measurements around the H α , H β , MgII and CIV regions, as well as other quantities such as radio properties, broad absorption line quasar (BALQSO) flags, disk emitters, etc. We also compile virial black hole (BH) mass estimates based on various calibrations. For the fiducial virial mass estimates we use the Vestergaard & Peterson (VP06) calibrations for H β and CIV, and our own calibration for MgII which is calibrated to match the VP06 H β masses on average. We describe the construction of this catalog, and discuss its limitations. The catalog and its future updates will be made publicly available online.

Subject headings: black hole physics — galaxies: active — quasars: general — surveys

1. INTRODUCTION

In recent years, studies of quasars and active galactic nuclei (AGNs) have been greatly facilitated by dedicated large-scale wide and deep field surveys in different bands, most notably by optical surveys such as the Sloan Digital Sky Survey (SDSS, York et al. 2000) and the 2QZ survey (Croom et al. 2004). Indeed, the growing body of data has revolutionized the study of quasars and AGNs. Large, homogeneous data sets allow detailed investigations of the phenomenological properties of quasars and AGNs, offering new insights to the central engine powering these objects and their connections to their host galaxies, especially when combined with multi-wavelength coverage. At the same time, it has become important to fit the quasar/AGN population into its cosmological context, i.e., how the supermassive black hole (SMBH) population evolves across cosmic time. These data have led to a coherent picture of the cosmic evolution of the SMBH population within the concordance Λ CDM paradigm (Kauffmann & Haehnelt 2000; Wyithe & Loeb 2003; Hopkins et al. 2006, 2008; Shankar et al. 2009; Shen 2009), where the key observational components are: quasar clustering, the luminosity function (LF), the BH mass function, and the correlations between BHs and their host properties. Increasingly larger data sets are offering unique opportunities to measure these properties with unprecedented precision.

In an earlier attempt to study the virial BH mass and Eddington ratio distributions of quasars, we measured spectral properties for the SDSS Data Release 5 (DR5) quasar catalog (Schneider et al. 2007; Shen et al. 2008b). We hereby extend this exercise to the DR7 quasar catalog (Schneider et al. 2010). Unlike our earlier version, we now include a more complete compilation of quantities from our spectral fits. Our measurements are more sophisticated than the SDSS pipeline outputs in many ways, and are hence of practical value. We describe the parent quasar sample in §2, the spectral measure-

ments and the catalog format in §3. We discuss possible applications of this catalog, as well as the caveats and limitations of our measurements in §4. Throughout this paper we use cosmological parameters $\Omega_{\Lambda} = 0.7$, $\Omega_0 = 0.3$ and $h = 0.7$.

2. THE SAMPLE

The SDSS uses a dedicated 2.5-m wide-field telescope (Gunn et al. 2006) with a drift-scan camera with 30 2048 \times 2048 CCDs (Gunn et al. 1998) to image the sky in five broad bands (*ugriz*; Fukugita et al. 1996). The imaging data are taken on dark photometric nights of good seeing (Hogg et al. 2001), are calibrated photometrically (Smith et al. 2002; Ivezić et al. 2004; Tucker et al. 2006) and astrometrically (Pier et al. 2003), and object parameters are measured (Lupton et al. 2001; Stoughton et al. 2002). Quasar candidates (Richards et al. 2002a) for follow-up spectroscopy are selected from the imaging data using their colors, and are arranged in spectroscopic plates (Blanton et al. 2003) to be observed with a pair of fiber-fed double spectrographs.

Our parent sample is the latest compilation of the spectroscopic quasar catalog (Schneider et al. 2010) from SDSS DR7 (Abazajian et al. 2009). This sample contains 105,783 bona fide quasars that are brighter than $M_i = -22.0$ and have at least one broad emission line with FWHM larger than 1000 km s⁻¹ or have interesting/complex absorption features. About half of these objects are selected uniformly using the final quasar target selection algorithm described in Richards et al. (2002a), with the remaining objects selected via early versions of target selection or various serendipitous algorithms (see Schneider et al. 2010), whose selection completeness cannot be readily quantified. For studies such as quasar clustering and the LF, one should use the uniformly selected quasar sample. Fig. 1 shows the distribution of the 105,783 quasars in the redshift-luminosity plane.

To include radio properties, we match the DR7 quasar catalog with the FIRST catalog⁶ (White et al. 1997) and estimate the radio loudness $R = f_{6\text{cm}}/f_{2500}$ following Jiang et al. (2007), where $f_{6\text{cm}}$ and f_{2500} are the flux density (f_{ν}) at rest-frame 6 cm and 2500 Å, respectively. The rest-frame 6 cm flux density is determined from the FIRST integrated flux density at 20 cm assuming a power-law slope of $\alpha_{\nu} = -0.5$; the rest-frame 2500

¹ Harvard-Smithsonian Center for Astrophysics, 60 Garden St., MS-51, Cambridge, MA 02138, USA.

² Dept. of Physics & Astronomy, York University, 4700 Keele St., Toronto, ON, M3J 1P3, Canada.

³ Department of Physics, Drexel University, 3141 Chestnut Street, Philadelphia, PA 19104.

⁴ Department of Astronomy and Astrophysics, 525 Davey Laboratory, Pennsylvania State University, University Park, PA 16802.

⁵ Princeton University Observatory, Princeton, NJ 08544.

⁶ The version of the FIRST source catalog and the coverage maps used are as of July 16, 2008 (<http://sundog.stsci.edu/first/catalogs/readme.html>).

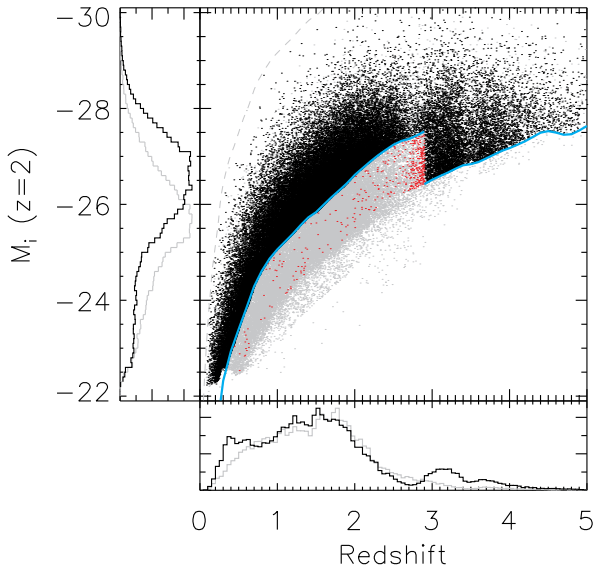


FIG. 1.— The distribution of DR7 quasars in luminosity-redshift space. The black dots are uniformly-selected quasars and the gray dots are quasars selected by a variety of earlier algorithms or serendipitous selections. The red dots are selected by the QSO_HIZ uniform selection but with $i > 19.1$ and at $z < 2.9$, and should be removed in constructing homogeneous quasar samples. The cyan lines show the corresponding (continuum and emission line) K -corrected, i -band absolute magnitude (normalized at $z = 2$) for $i = 19.1$ ($z < 2.9$) and $i = 20.2$ ($z > 2.9$) respectively, and the gray dashed line shows that for $i = 15$ (the bright limit for SDSS quasar targets). The non-uniformly selected quasars (gray dots) are targeted to fainter luminosities than the uniformly selected quasars.

Å flux density is determined from the power-law continuum fit to the spectrum as described in §3. We have followed Jiang et al. (2007) to crudely determine core-dominant and lobe-dominant radio morphology for FIRST detected quasars.

The reduced 1D spectral data used in this study are available through the DAS⁷. The spectral resolution is $R \sim 1850$ – 2200 , and the 1D spectra are stored in vacuum wavelength, with a pixel scale 10^{-4} in log-wavelength, which corresponds to ~ 69 km s⁻¹. Since DR6 (Adelman-McCarthy et al. 2008), the spectral flux calibration is scaled to the PSF magnitudes of standard stars, therefore there is no longer need for a fiber-to-PSF conversion for the spectral flux (Shen et al. 2008 already used the PSF spectral flux calibration). Throughout the paper, we refer to the signal-to-noise ratio per pixel as S/N.

To flag BALQSOs, we use the Gibson et al. (2009) DR5 BALQSO catalog to set the CIV and MgII BALQSO flags (using their “BIO” flags). We also visually inspected all the post-DR5 quasars with redshift $z > 1.45$ to identify obvious CIV BALQSOs (we may have missed some weak BALQSOs). We did not perform a systematic search for low-ionization MgII BALQSOs because of the large number of quasars with MgII coverage and the much rarer occurrence of MgII BALQSOs. Although we report serendipitously identified MgII BALQSOs, the completeness of these objects is low. We identified a total of 6214 BALQSOs in the DR7 quasar catalog.

3. SPECTRAL MEASUREMENTS

We are primarily interested in the broad $H\alpha$, $H\beta$, MgII, and CIV emission lines because these are the most frequently studied lines that are available for a wide range of redshifts, and more importantly, have been calibrated as virial black hole (BH) mass estimators (e.g., Vestergaard 2002; McLure

& Jarvis 2002; McLure & Dunlop 2004; Greene & Ho 2005b; Vestergaard & Peterson 2006; McGill et al. 2008; Vestergaard & Osmer 2009; Wang et al. 2009b). Measurements of other spectral lines will be reported in future updates of this value-added product.

There are numerous studies of the statistical emission line properties of quasars relying either on direct measurements, or on spectral fits of the line profile (e.g., Boroson & Green 1992; Marziani et al. 1996; McLure & Jarvis 2002; Richards et al. 2002b; McLure & Dunlop 2004; Bachev et al. 2004; Dietrich & Hamann 2004; Baskin & Laor 2005; Kollmeier et al. 2006; Fine et al. 2006, 2008; Bonning et al. 2007; Salvander et al. 2007; Sulentic et al. 2007; Shen et al. 2008a,b; Hu et al. 2008a,b; Zamfir et al. 2009; Wang et al. 2009b; Wu et al. 2009; Dong et al. 2009b,a). For the same set of data, different studies sometimes report different results for certain measured quantities due to the different line-measure techniques used in these studies. Which method is preferred, however, depends on the nature of the problem under study. A classic example is measuring the *full-width-at-half-maximum* (FWHM) in estimating the BH mass using virial estimators, where the usual complications are: 1) how to subtract the continuum underneath the line; 2) how to treat the narrow line component (especially for MgII and CIV); 2) how to measure the broad line profile. These choices crucially depend on the particular virial estimator calibrations used, e.g., new methods of FWHM measurements must be re-calibrated either against reverberation mapping masses or internally between different line estimators. On the other hand, different line-measure methods have different sensitivities to the quality of the spectra (spectral resolution and S/N), which introduce systematics when switching from high-quality to low-quality data (e.g., Denney et al. 2009). It is beyond our scope to fully settle these issues within the current study.

We remove the effects of Galactic extinction in the SDSS spectra using the Schlegel et al. (1998) map and a Milky Way extinction curve from Cardelli et al. (1989) with $R_V = 3.1$, and shift the spectra to rest-frame using the cataloged redshift as the systemic redshift. For each line, we fit a local power-law continuum ($f_\lambda = A\lambda^{\alpha_\lambda}$) plus an iron template (Boroson & Green 1992; Vestergaard & Wilkes 2001; Salvander et al. 2007) to the wavelength range around the line that is not contaminated by the broad line emission. During the continuum+iron fitting we simultaneously fit five parameters: the normalization A and slope α_λ of the power-law continuum, the normalization A_{Fe} , line broadening σ_{Fe} and velocity offset v_{Fe} relative to the systemic redshift for the iron template fit. Because of the moderate spectral quality of SDSS spectra (median $S/N \lesssim 10$) σ_{Fe} and v_{Fe} are often poorly constrained; nevertheless the iron fit gives a reasonably good estimate of the iron flux to be subtracted off. The continuum+iron fit is then subtracted from the spectrum, and the resulting line spectrum is modelled by various functions. In the case of $H\alpha$ and $H\beta$ the narrow emission lines, e.g., [O III] $\lambda\lambda 4959, 5007$, [N II] $\lambda\lambda 6548, 6584$, [S II] $\lambda\lambda 6717, 6731$, are also fit simultaneously. Below we describe the detailed fitting procedures for the four broad lines.

3.1. $H\alpha$

For $H\alpha$ we use the optical iron template from Boroson & Green (1992), and we fit for objects with $z \leq 0.39$. The continuum+iron fitting windows are $[6000, 6250]$ Å and $[6800, 7000]$ Å.

⁷ <http://das.sdss.org/spectro/>

For $H\alpha$ line fitting, we fit the wavelength range [6400,6800] Å. The narrow components of $H\alpha$, $[N\text{II}]\lambda\lambda 6548,6584$, $[S\text{II}]\lambda\lambda 6717,6731$ are each fit with a single Gaussian. Their velocity offsets from the systemic redshift and line widths are tied to be the same, and the relative flux ratio of the two $[N\text{II}]$ components is fixed to 2.96. We impose an upper limit on the narrow line FWHM $< 1200\text{ km s}^{-1}$ (e.g., Hao et al. 2005). The broad $H\alpha$ component is modelled in two ways: 1) a single Gaussian; 2) multiple Gaussians (up to three). The second method yields similar results to the fits with a truncated Gaussian-Hermite function (e.g., van der Marel & Franx 1993). During the fitting, all lines are restricted to be emission lines (i.e., positive flux).

3.2. $H\beta$

For $H\beta$ we use the optical iron template from Boroson & Green (1992), and we fit for objects with $z \leq 0.89$. The continuum+iron fitting windows are [4435,4700] Å and [5100,5535] Å. For the $H\beta$ line fitting, we follow a similar procedure as $H\alpha$ to fit for $H\beta$ and $[O\text{III}]\lambda\lambda 4959,5007$, where the line fitting wavelength range is [4700,5100] Å. Since the $[O\text{III}]\lambda\lambda 4959,5007$ lines frequently show asymmetric blue wings (e.g., Heckman et al. 1981; Greene & Ho 2005a; Komossa et al. 2008) and sometimes even more dramatic double-peaked profiles (e.g., Liu et al. 2010; Smith et al. 2009; Wang et al. 2009a), we model each of the narrow $[O\text{III}]\lambda\lambda 4959,5007$ lines with two Gaussians, one for the core and the other for the blue wing. The velocity offset and FWHM of the narrow $H\beta$ line are tied to those of the core $[O\text{III}]\lambda\lambda 4959,5007$ components, and we impose an upper limit of 1200 km s^{-1} on the narrow line FWHM. As in the $H\alpha$ case, the broad $H\beta$ component is modelled either by 1) a single Gaussian; or 2) multiple Gaussians (up to three).

The single Gaussian fit to the broad component is essentially the same as we did in Shen et al. (2008b), and is somewhat similar to the procedure in McLure & Dunlop (2004)⁸. However, in many objects the broad $H\alpha/H\beta$ component cannot be fit perfectly with a single Gaussian; and FWHMs from the single Gaussian fits are systematically larger by ~ 0.1 dex than those from the multiple Gaussian fits (e.g., Shen et al. 2008b). The additional multiple Gaussian fits for the broad $H\alpha/H\beta$ component provide a better fit to the overall broad line profile, and the FWHM measured from the model flux can be used in customized virial calibrations. It is unclear, however, which FWHM is a better surrogate for the virial velocity, that is, the one that yields the smallest scatter in the calibration against reverberation mapping (RM) masses.

3.3. $Mg\text{II}$

For $Mg\text{II}$ we use the UV iron template from Vestergaard & Wilkes (2001), and we fit for objects with $0.35 \leq z \leq 2.25$. The continuum+iron fitting windows are [2200,2700] Å and [2900,3090] Å. We then subtract the pseudo-continuum from the spectrum, and fit for the $Mg\text{II}$ line over the [2700,2900] Å wavelength range, with a single Gaussian (with FWHM $< 1200\text{ km s}^{-1}$) for the narrow $Mg\text{II}$ component, and for the broad $Mg\text{II}$ component with: 1) a single Gaussian; 2) multiple Gaussians (up to three). Again, the multiple-Gaussian fits often provide a better fit to the overall broad $Mg\text{II}$ profile; but we

⁸ In addition to Gaussian profiles, McLure & Dunlop (2004) also tried to fit the broad/narrow component with a single Lorentzian, but this does not change the measured broad FWHM significantly.

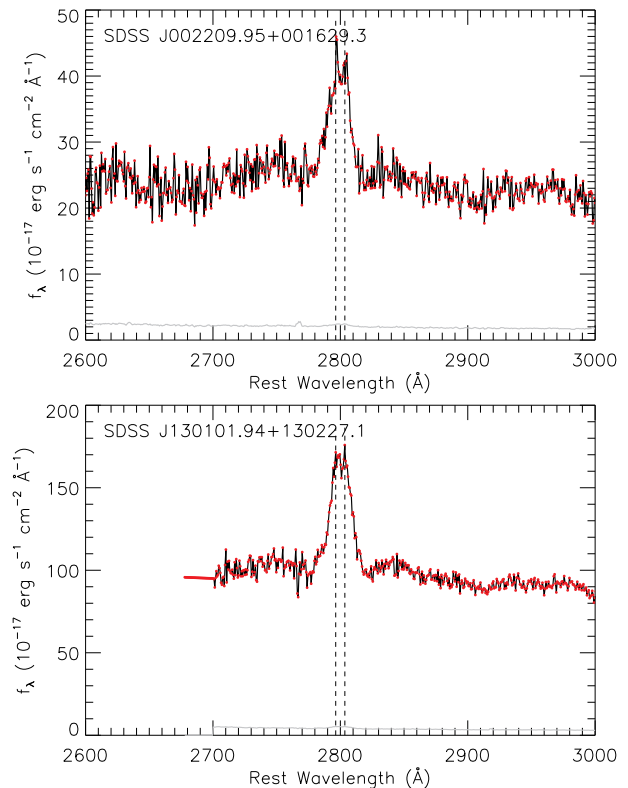


FIG. 2.— Two examples of $Mg\text{II}$ lines which show narrow line components. The spectra are plotted as black lines with the data points superposed (red dots). The gray lines show the errors. The dashed vertical lines mark the locations of the $Mg\text{II} \lambda\lambda 2796,2803$ doublet.

have retained the FWHMs from a single Gaussian fit in order to use the $Mg\text{II}$ virial mass calibrations in McLure & Jarvis (2002) and McLure & Dunlop (2004). Some $Mg\text{II}$ virial estimator calibrations (e.g., McLure & Jarvis 2002; McLure & Dunlop 2004; Wang et al. 2009b) do subtract a narrow $Mg\text{II}$ component while others (e.g., Vestergaard & Osmer 2009) do not. To utilize the $Mg\text{II}$ calibration in Vestergaard & Osmer (2009), we also measure the FWHMs from the broad+narrow $Mg\text{II}$ fits (with multiple Gaussians for the broad component), where any Gaussian component having flux less than 5% of the total line flux is rejected when computing the FWHM — this step is to eliminate artificial noise spikes which can bias the FWHM measurements. During our fitting, we mask out 3σ outliers below the 20-pixel boxcar-smoothed spectrum to reduce the effects of narrow absorption troughs.

Unlike the cases of $H\alpha$ and $H\beta$, it is somewhat ambiguous whether it is necessary to subtract a narrow line component for $Mg\text{II}$ and if so, how to do it. On one hand, for some objects, such as SDSSJ002209.95+001629.3 and SDSSJ130101.94+130227.1 (e.g., Fig. 2), the spectral quality is sufficient to see the bifurcation of the $Mg\text{II}$ doublet around the peak. The locations of the two peaks indicate that they are associated with the $Mg\text{II} \lambda\lambda 2796,2803$ doublet, and the fact that they are resolved means that the FWHM of each component is $\lesssim 750\text{ km s}^{-1}$, hence they are most likely associated with the narrow line region. On the other hand, such cases are rare and most SDSS spectra do not have adequate S/N to unambiguously locate the narrow $Mg\text{II}$ doublet. Associated narrow $Mg\text{II}$ absorption troughs can further complicate the situation by mimicking two peaks. Hence although our approach of fitting a single Gaussian to the narrow $Mg\text{II}$ component is not perfect, it nevertheless accounts for some narrow

MgII contamination. Fig. 3 compares our broad MgII FWHM measurements with those from Wang et al. (2009b) for the objects in both studies. Although we have used a different approach, our results are consistent with theirs, with a mean offset ~ 0.05 dex. This systematic offset between our results and theirs is caused by the fact that they are treating the broad MgII line as a doublet as well, while we (and most studies) are treating the broad MgII line as a single component.

3.4. CIV

For CIV we fit for objects with $1.5 \leq z \leq 4.95$. Iron emission is generally weak for CIV, and most of our objects do not have the spectral quality sufficient for a reliable iron template subtraction (e.g., Shen et al. 2008b). The power-law continuum fitting windows are: [1445,1465] Å and [1700,1705] Å. We found fitting CIV with iron subtraction does not change the fitted CIV FWHM significantly, but systematically reduces the CIV EW by ~ 0.05 dex when the iron flux under the wings of the CIV line is accounted for. At the same time, fitting iron emission increases the scatter in the fitted continuum slope and normalization, due to imperfect subtraction of the iron flux. Therefore we report our CIV measurements without the iron template fits, and emphasize that the CIV EWs may be overestimated by ~ 0.05 dex on average.

The continuum subtracted line emission within [1500,1600] Å was fitted with three Gaussians (e.g., Shen et al. 2008b), and we measure the line FWHM from the model fit. To reduce the effects of noise spikes, we reject any Gaussian component having flux less than 5% of the total model flux when computing the FWHM. However, unlike some attempts in the literature (e.g., Bachev et al. 2004; Baskin & Laor 2005; Sulentic et al. 2007; Zamfir et al. 2009), we do not subtract a narrow CIV component because: 1) it is still debatable if a strong narrow CIV component exists for most quasars, or if it is feasible to do such a subtraction; 2) existing CIV virial estimators are calibrated using the FWHMs from the entire CIV profile (Vestergaard & Peterson 2006).

Many CIV lines are affected by narrow or broad absorption features. To reduce the effects of such absorption on the CIV fits, we mask out 3σ outliers below the 20-pixel boxcar-smoothed spectrum during our fits (to remedy for narrow absorption features); we also perform a second fit excluding pixels below 3σ of the first model fit, and replace the first one if statistically justified (to remedy for broad absorption features). We found these recipes can minimize the impact of narrow or moderate absorption features, but the improvement is marginal for objects severely affected by broad absorption.

3.5. Reliability of spectral fits and error estimation

Our spectral fits were performed in an automatic fashion. Upon visual inspection of the fitting results we are confident that the vast majority of the fits to high S/N spectra were successful, and comparisons with independent fits by others also show good agreement. However, the reliability of our spectral fits drops rapidly for low-quality spectra. Fig. 4 shows the distributions of the median S/N per pixel around the line-fitting region for objects that have line measurements, for H β , MgII and CIV respectively. Although the bulk of objects have median S/N > 5 for the line-fitting regions, there are many objects that have lower median S/N, especially for CIV at high redshift. The effects of S/N on the measurements depend on both the properties of the lines (i.e., line profile, line strength, degree of absorption features, etc), and the line-fitting tech-

nique itself (i.e., what function form used, how to deal with absorption troughs, etc).

To investigate the impact of S/N on our fitting parameters we ran a series of Monte Carlo simulations. We select representative real spectra with high S/N, then degrade the spectra by adding Gaussian noise and measure the line properties using the same line-fitting routine. For each line (H β , MgII, or CIV), we study several objects with various line shapes and EWs. We simulate 500 trials for each S/N level and take the median and the 68% range as the measurement result and its error.

Figs. 5-7 show several examples of our investigations for H β , MgII and CIV respectively. As expected, decreasing the S/N ratio increases measurement scatter. In all cases the fitted continuum is unbiased as S/N decreases. The FWHMs and EWs are biased by less than $\pm 20\%$ as S/N is reduced to as low as ~ 3 only for the high-EW cases. For low-EW cases, the FWHMs and EWs are biased low/high by $> 20\%$ for S/N $\lesssim 5$. Since the median EWs for the three lines are > 30 Å (see Figs. 10-12), we expect that the measurements for most objects are unbiased to within $\pm 20\%$ down to S/N ~ 3 . But for many purposes, it would be more conservative to impose a cut at S/N > 5 for reliable measurements.

Finally, to estimate the uncertainties in the measured quantities in our fits, we generate 50 mock spectra for each object using the flux errors and fit for those mock spectra with the same fitting routines. We estimate the measurement uncertainties from the 68% range (centered on the median) of the distributions of fitting results of the 50 trials.

3.6. Host galaxy contamination

For the vast majority of objects in our catalog with $z \gtrsim 0.5$, host galaxy contamination is negligible. However, for the $z \lesssim 0.5$ low-luminosity quasars in our sample, the continuum luminosity at restframe 5100Å may be contaminated by light from the host galaxies. Unfortunately the spectral quality of the majority of individual objects does not allow a reliable galaxy continuum subtraction. Here we estimate the effects of host contamination with stacked spectra.

We take all quasars with measurable rest frame 5100Å continuum luminosity, L_{5100} , and bin them on a grid of $\Delta \log L_{5100} = 0.1$ for $\log(L_{5100}/\text{ergs}^{-1}) = 44.1 - 45.5$. Following Vanden Berk et al. (2001), we generate geometric mean composite spectra for objects in each luminosity bin. The composite spectra are shown in Fig. 8, where the flux gradually flattens at long wavelengths due to increasing host contamination at fainter luminosities. This trend is accompanied by the increasing prominence of stellar absorption features and narrow line emission towards fainter luminosities. The inset shows the fractional host contamination at 5100Å assuming that the highest luminosity bin ($\log L_{5100} = 45.5$) is not affected by the host and that the intrinsic AGN power-law continuum slope does not change over the luminosity range considered. The host contamination is substantial at $\log L_{5100} < 44.5$, and becomes negligible towards higher luminosities. The median value of $\log L_{5100}$ for quasars in this low-redshift sample is ~ 44.6 , and therefore the host contamination on average is $\sim 15\%$, which leads to a ~ 0.06 dex overestimation of the 5100Å continuum luminosity and thus ~ 0.03 dex overestimation of the H β -based virial masses for the median object. While we do not correct the measured 5100Å continuum luminosity (and other quantities depending on it) in the catalog, we provide an empirical fitting formula of

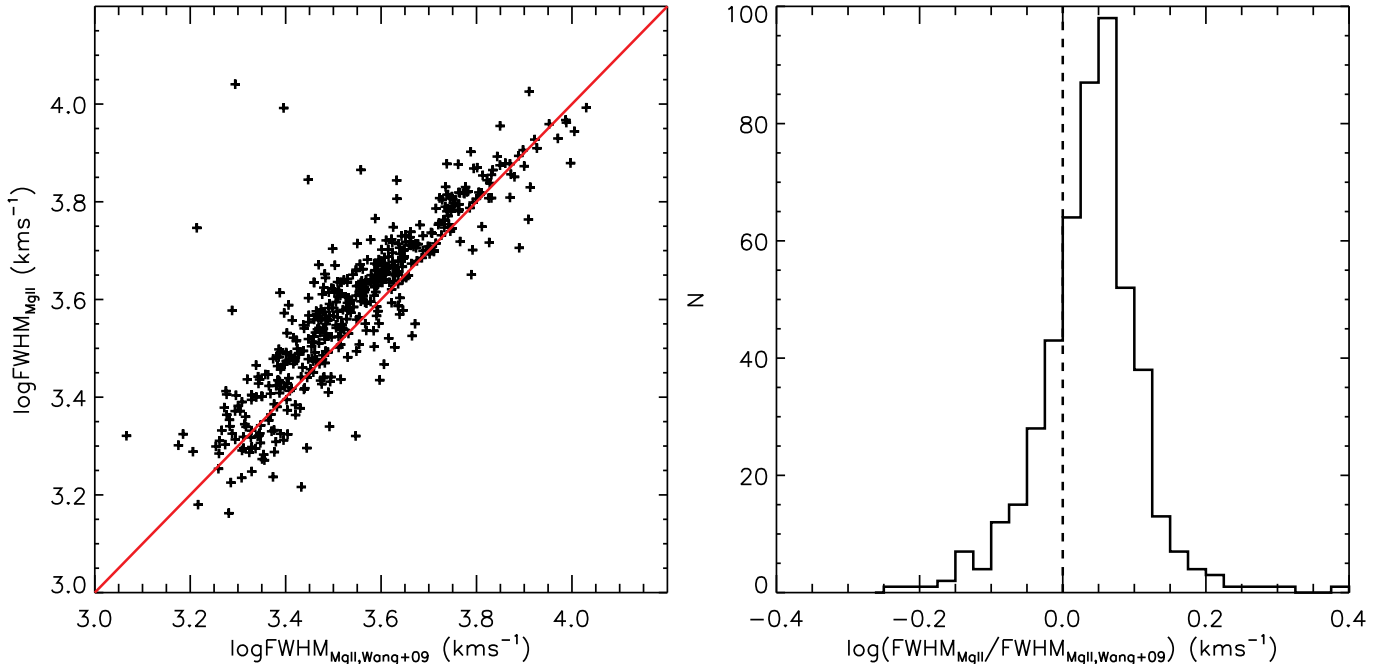


FIG. 3.— Comparison of our MgII FWHMs with those from Wang et al. (2009b) for the same objects. The left panel shows a one-to-one scatter plot, where the solid line is the unity relation. The right panel shows a histogram of the ratio between the two values. Our broad MgII FWHM values are systematically larger by ~ 0.05 dex than those in Wang et al. (2009b), mainly caused by the fact that they fit the broad MgII as a doublet while we did not.

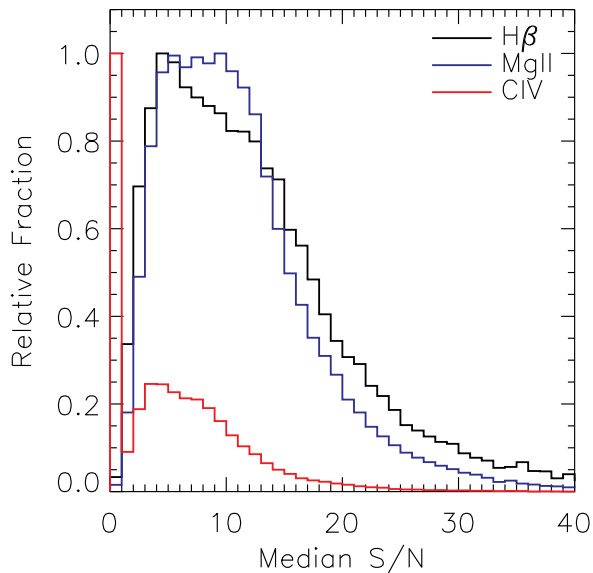


FIG. 4.— Distributions of the median S/N per pixel for objects with measurements around the line-fitting regions for $H\beta$, MgII and CIV.

the average host contamination based on the stacked spectra (dashed line in the inset of Fig. 8):

$$\frac{L_{5100,\text{host}}}{L_{5100,\text{QSO}}} = 0.8052 - 1.5502x + 0.9121x^2 - 0.1577x^3 \quad (1)$$

for $x+44 \equiv \log L_{5100,\text{total}} < 45.053$; no correction is needed for luminosities above this value.

We suspect that host contamination is largely responsible for the apparent anti-correlation between L_{5100} and spectral slope, and the “negative” Baldwin effect for $H\beta$ below $L_{5100} \sim 10^{45}$ ergs $^{-1}$ seen in Fig. 10.

3.7. The spectral catalog

We have tabulated all the measured quantities from the spectral fitting in the online catalog of this paper, along with other properties⁹. The current compilation extends our earlier DR5 compilation (Shen et al. 2008b) by including the post-DR5 quasars, as well as measurements based on new multiple-Gaussian fits to the lines (as discussed earlier). The format of the catalog is described in Table 1. Objects are in the same order as the DR7 quasar catalog in Schneider et al. (2010). Below we describe the specifics of the cataloged quantities. The SDSS terminology can be found on the SDSS website¹⁰. Flux measurements were corrected neither for intrinsic extinction and reddening, nor for host contaminations.

1. SDSS DR7 designation: *hhmms.ss+ddmms.s* (J2000.0; truncated coordinates)

2-4. RA and DEC (in decimal degrees, J2000.0), redshift. Here the redshifts are taken from the DR7 quasar catalog (Schneider et al. 2010). Hewett & Wild (2010) provided improved redshifts for SDSS quasars. These improved redshifts are particularly useful for generating coadded spectra, but the cataloged DR7 redshifts are fine for most of the purposes considered in here.

5-7. Spectroscopic plate, fiber and MJD: the combination of plate-fiber-MJD locates a particular spectroscopic observation in SDSS. The same object can be observed more than once with different plate-fiber-MJD combinations either on a repeated plate (same plate and fiber numbers but different MJD number), or on different plates.

⁹ Note that in Shen et al. (2008b) we only reported high-quality measurements with median S/N > 6 and a reduced $\chi^2 < 5$ for a single-Gaussian fit to the line; here we retain all measurements for completeness.

¹⁰ <http://www.sdss.org/dr7/>

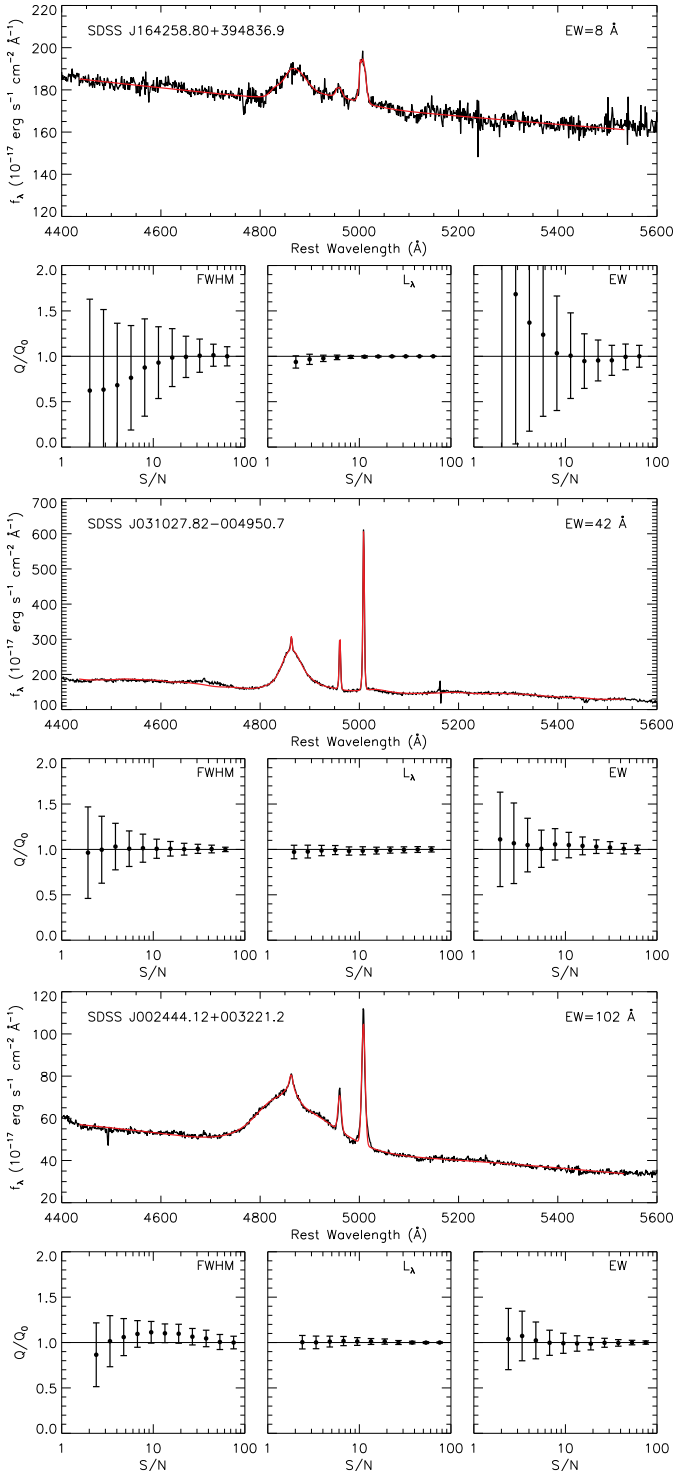


FIG. 5.— Effects of S/N on the line measurements for $H\beta$ for three representative examples. For each object we show the actual spectrum (black line) and the best-fit model (red line) in the upper panel. The lower three panels show the ratios of the values measured from the degraded spectra to those measured from the original spectrum, as functions of S/N; black dots are median values and the error bars indicate the 68% quantile.

8. TARGET_FLAG_TARGET: the target selection flag (TARGET version).
9. N_{spec} : number of spectroscopic observations. While we only used the default spectrum in our spectral fitting, this flag indicates if there are multiple spectroscopic observations for each object.

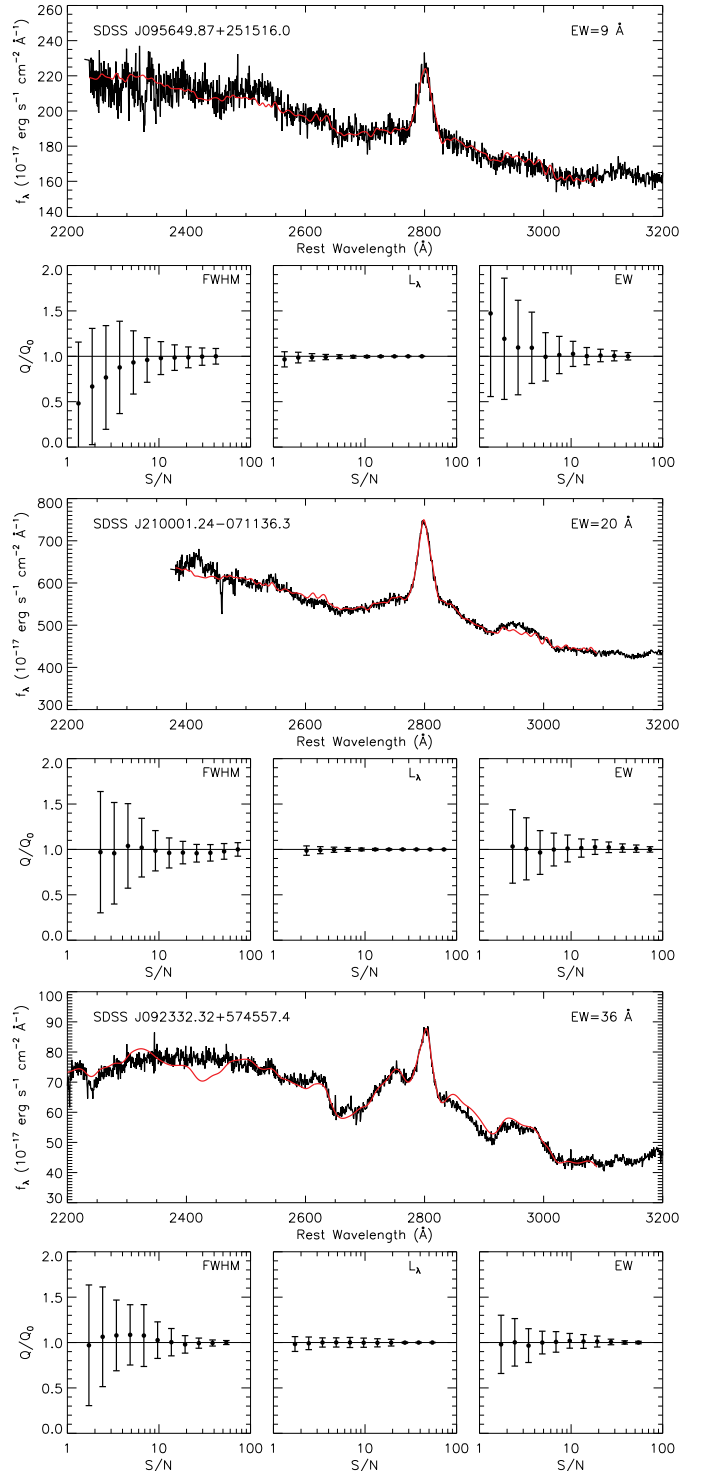


FIG. 6.— Effects of S/N on the line measurements for $MgII$ for three representative examples. For each object we show the actual spectrum (black line) and the best-fit model (red line) in the upper panel. The lower three panels show the ratios of the values measured from the degraded spectra to those measured from the original spectrum, as functions of S/N; black dots are median values and the error bars indicate the 68% quantile.

10. Uniform flag. 0=not in the uniform sample¹¹; 1=uniformly selected using the target selection algorithm in Richards et al. (2002a), and flux limited to $i = 19.1$ at $z < 2.9$ and $i = 20.2$ at $z > 2.9$; 2=selected by the

¹¹ For more details regarding the uniform sample selection and its sky coverage, see Richards et al. (e.g., 2002a, 2006b); Shen et al. (e.g., 2007).

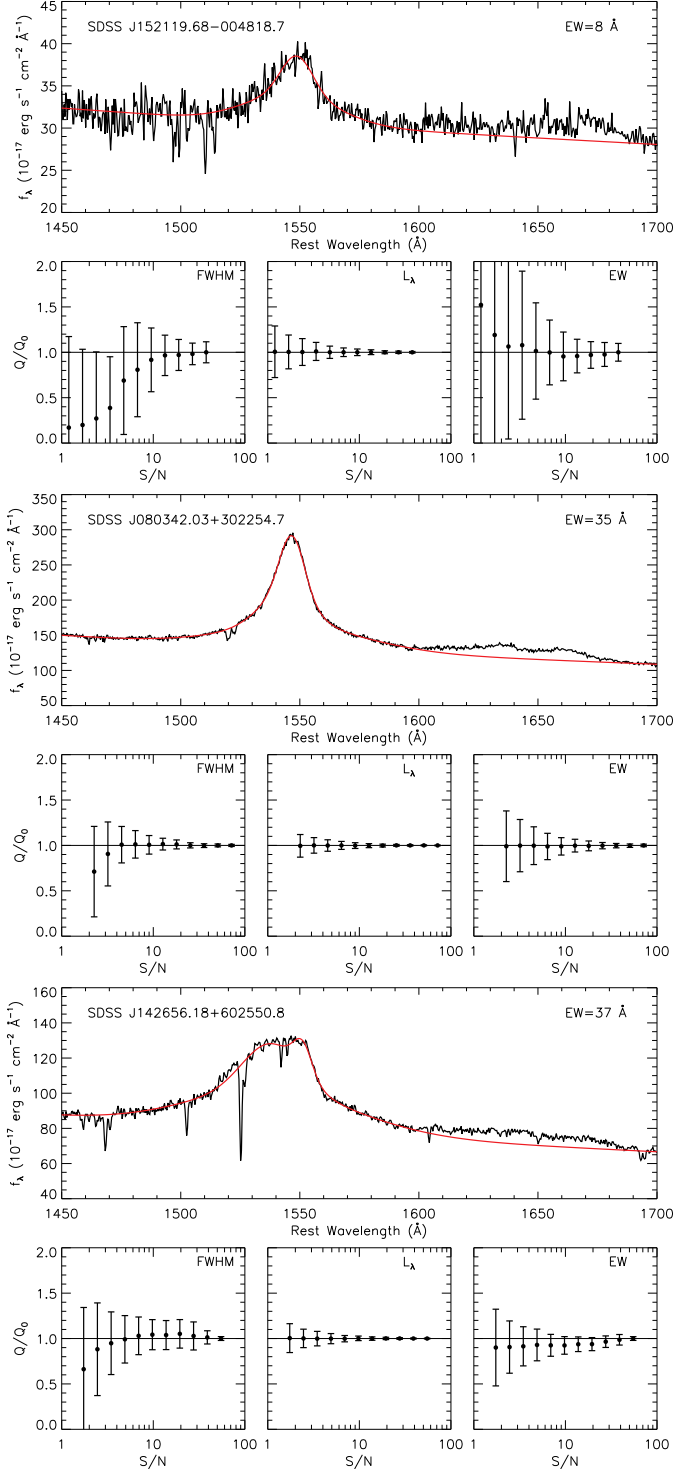


FIG. 7.— Effects of S/N on the line measurements for CIV for three representative examples. For each object we show the actual spectrum (black line) and the best-fit model (red line) in the upper panel. The lower three panels show the ratios of the values measured from the degraded spectra to those measured from the original spectrum, as functions of S/N; black dots are median values and the error bars indicate the 68% quantile. Note that the HeII/OIII complex around 1650Å is not fitted.

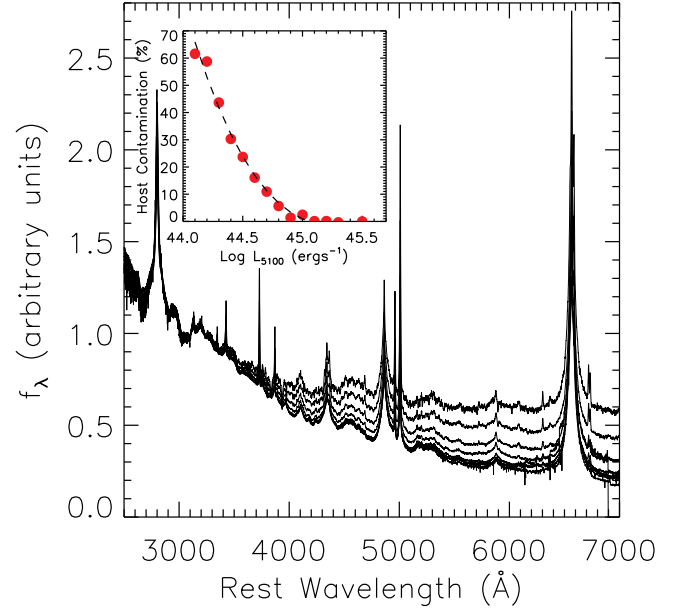


FIG. 8.— Composite spectra for objects binned in $\log L_{5100}$, normalized at 3000Å. The flux gradually flattens at long wavelength due to the increasing host contamination towards fainter luminosities, accompanied by the increasing prominence of stellar absorption features and narrow line emission. The inset shows the fractional host contamination at 5100Å assuming that the highest luminosity bin ($\log L_{5100} = 45.5$) is not affected by host emission and that the intrinsic AGN power-law continuum slope does not change over the luminosity range considered. The dashed line in the inset is a polynomial fit (Eqn. 1).

QSO_HiZ branch only in the uniform target selection (Richards et al. 2002a) and with measured spectroscopic redshift $z < 2.9$ and $i > 19.1$. Objects with uniform flag=2 are selected by the uniform quasar target algorithm, but should not be included in statistical studies; the fraction of such uniform objects is low ($< 1\%$).

11. $M_i(z=2)$: absolute i -band magnitude in the current cosmology, K -corrected to $z=2$ following¹² Richards et al. (2006b).
- 12-13. Bolometric luminosity L_{bol} and its error: computed from L_{5100} ($z < 0.7$), L_{3000} ($0.7 \leq z < 1.9$), L_{1350} ($z \geq 1.9$) using the spectral fits and bolometric corrections¹³ $BC_{5100} = 9.26$, $BC_{3000} = 5.15$ and $BC_{1350} = 3.81$ from the composite SED in Richards et al. (2006a).
14. BAL flag: 0=nonBALQSO or no wavelength coverage; 1=CIV HiBALQSO; 2=MgII LoBALQSO; 3=both 1 and 2. The LoBALQSO selection is very incomplete as discussed in §2.

¹² The K -corrections here include both continuum K -correction and emission-line K -correction (Richards et al. 2006b); while the cataloged absolute magnitudes in Schneider et al. (2010) were K -corrected for continuum only.

¹³ The SEDs for individual quasars show significant scatter (e.g., Richards et al. 2006a), so the adopted bolometric corrections are only appropriate in the average sense. Some authors suggest to remove the IR bump in the SED in estimating the bolometric corrections (e.g., Marconi et al. 2004), where the IR radiation is assumed to come from the reprocessed UV radiation. This will generally reduce the bolometric corrections by about one third. Integrating the mean SED in Richards et al. (2006a) from 1 μm to 10 keV for the bolometric luminosity we obtain: $BC_{5100} = 5.47$, $BC_{3000} = 3.04$ and $BC_{1350} = 2.25$. However, since we are not correcting for intrinsic extinction of the flux, using our fiducial bolometric corrections will not overestimate the bolometric luminosity significantly.

15. FIRST radio flag: -1 =not in FIRST footprint; 0 =FIRST undetected; 1 =core dominant; 2 =lobe dominant (for details, see Jiang et al. 2007).
- 16-17. *Observed* radio flux density at rest-frame 6 cm $f_{6\text{cm}}$ and optical flux density at rest-frame 2500 Å f_{2500} .
18. Radio loudness $R \equiv f_{6\text{cm}}/f_{2500}$.
- 19-24. L_{5100} , L_{3000} , L_{1350} and their errors: continuum luminosity at 5100 Å, 3000 Å and 1350 Å, measured from the spectral fits. No correction for host contamination is made (see discussion in §3.6).
- 25-30. Line luminosity, FWHM, equivalent width and their errors for the broad $H\alpha$ component.
- 31-36. Line luminosity, FWHM, equivalent width and their errors for the narrow $H\alpha$ component.
- 37-40. Line luminosity, equivalent width and their errors for narrow $[\text{N II}] \lambda 6584$.
- 41-44. Line luminosity, equivalent width and their errors for narrow $[\text{S II}] \lambda 6717$.
- 45-48. Line luminosity, equivalent width and their errors for narrow $[\text{S II}] \lambda 6731$.
- 49-50. 6000-6500 Å iron equivalent width and its error.
- 51-52. Power-law slope α_λ and its error for the continuum fit for $H\alpha$.
- 53-54. Number of good pixels and median S/N per pixel for the $H\alpha$ region (6400-6765 Å).
55. Reduced χ^2 for the $H\alpha$ line fit; -1 if not fitted.
- 56-61. Line luminosity, FWHM, equivalent width and their errors for the broad $H\beta$ component.
- 62-67. Line luminosity, FWHM, equivalent width and their errors for the narrow $H\beta$ component.
68. FWHM of broad $H\beta$ using a single Gaussian fit (Shen et al. 2008b).
- 69-72. Line luminosity, equivalent width and their errors for $[\text{O III}] \lambda 4959$.
- 73-76. Line luminosity, equivalent width and their errors for $[\text{O III}] \lambda 5007$.
- 77-78. 4435-4685 Å iron equivalent width and its error.
- 79-80. Power-law slope α_λ and its error for the continuum fit for $H\beta$.
- 81-82. Number of good pixels and median S/N per pixel for the $H\beta$ region (4750-4950 Å).
83. Reduced χ^2 for the $H\beta$ line fit; -1 if not fitted.
- 84-89. Line luminosity, FWHM, equivalent width and their errors for the whole Mg II profile.
- 90-95. Line luminosity, FWHM, equivalent width and their errors for the broad Mg II profile.
96. FWHM of broad Mg II using a single Gaussian fit (Shen et al. 2008b).
- 97-98. 2200-3090 Å iron equivalent width and its error.
- 99-100. Power-law slope α_λ and its error for the continuum fit for Mg II .
- 101-102. Number of good pixels and median S/N per pixel for the Mg II region (2700-2900 Å).
103. Reduced χ^2 for the Mg II line fit; -1 if not fitted.
- 104-109. Line luminosity, FWHM, equivalent width and their errors for the whole C IV profile.
- 110-111. Power-law slope α_λ and its error for the continuum fit for C IV .
- 112-113. Number of good pixels and median S/N per pixel for the C IV region (1500-1600 Å).
114. Reduced χ^2 for the C IV line fit; -1 if not fitted.
- 115-126. Velocity shifts (and their errors) relative to the systemic redshift (cataloged in Schneider et al. 2010) for broad $H\alpha$, narrow $H\alpha$, broad $H\beta$, narrow $H\beta$, broad Mg II , and C IV . The velocity shifts for the broad lines are measured from the peak of the multiple-Gaussian model fit to the broad component¹⁴. Recall that the velocity shifts of narrow lines were tied together during spectral fits. These velocity shifts can be used to compute the relative velocity offsets between two lines for the same object, such as the C IV - Mg II blueshift, but should *not* be interpreted as the velocity shifts from the restframe of the host galaxy due to uncertainties in the systemic redshift. Positive values indicate blueshift and negative values indicate redshift; value of 3×10^5 indicates an unmeasurable quantity.
- 127-138. Virial BH masses using calibrations of $H\beta$ (MD04), $H\beta$ (VP06), Mg II (MD04), Mg II (VO09), Mg II (S10) and C IV (VP06). The definitions of the acronym names of each calibration can be found in §4.3. Zero value indicates an unmeasurable quantity. We use FWHMs from a single Gaussian fit to the broad component for $H\beta$ (MD04) and Mg II (MD04); FWHMs from the multiple-Gaussian fit to the broad $H\beta$ for $H\beta$ (VP06); FWHMs from the multiple-Gaussian fit to the entire Mg II and C IV lines for Mg II (VO09) and C IV (VP06) respectively; FWHMs from the multiple-Gaussian fit to the broad Mg II line for Mg II (S10). See §3 and §4.3 for more details.
139. The adopted fiducial virial BH mass if more than one estimate is available. See detailed discussion in §4.3.
140. The measurement uncertainty of the adopted fiducial virial BH mass, propagated from the measurement uncertainties of continuum luminosity and FWHM. Note that this uncertainty neither includes the statistical uncertainty ($\gtrsim 0.3$ – 0.4 dex) from virial mass calibrations, nor includes the systematic uncertainties with these virial BH masses.

¹⁴ The velocity shifts of the broad lines measured from the centroid of a single Gaussian fit to the line on average are consistent with those using the peak of the multiple-Gaussian fit with negligible mean offset, but they can differ (typically by $\lesssim 200 \text{ km s}^{-1}$) for individual objects.

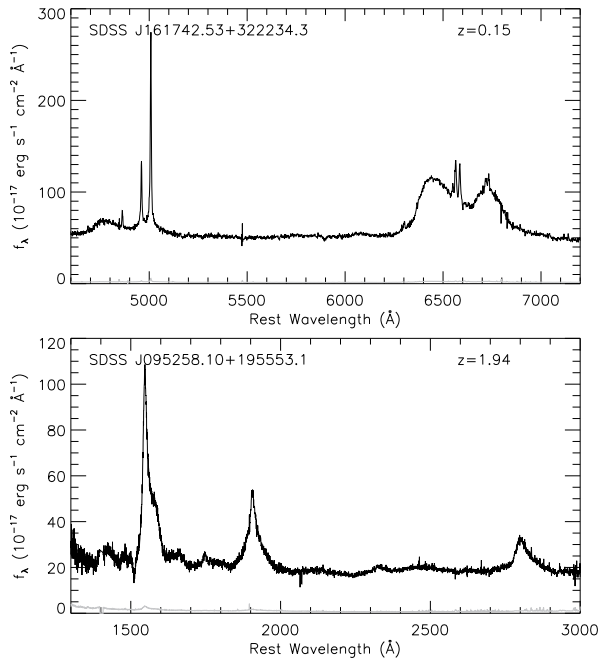


FIG. 9.— Two examples of disk emitters. *Upper*: a Balmer disk emitter at $z = 0.15$. *Bottom*: a possible CIV disk emitter at $z = 1.94$.

141. Eddington ratio computed using the fiducial virial BH mass.
142. Special interest flag. This is a binary flag: bit#0 set=disk emitters with high confidence (the vast majority are selected based on the Balmer lines); bit#1 set=disk emitter candidates; bit#2 set=double-peaked [O III] $\lambda\lambda 4959, 5007$ lines. These flags were set upon visual inspection of all $z < 0.89$ quasars in the catalog. In particular, disk emitter candidates (bit#1=1) are those with asymmetric broad Balmer line profile or systematic velocity shifts from the narrow lines. Fig. 9 shows two examples of disk emitters.

4. APPLICATIONS

The spectral measurements described above can be used to study the statistical properties of broad line quasars. Here we discuss several applications of this spectral catalog.

4.1. Correlations between emission line properties

One great virtue of the SDSS DR7 quasar survey is that it provides unprecedented statistics for broad-line quasar properties. To demonstrate this, Figs. 10-12 show some statistical properties of quasars using our spectral measurements for H β , MgII, and CIV, respectively. These figures show the typical values of these properties for SDSS quasars as a quick reference.

There are some correlations among the properties shown in Figs. 10-12 which are not due to selection effects, such as the well-known Baldwin effect (Baldwin 1977), and the correlations between EW and FWHM for MgII (e.g., Dong et al. 2009b). The statistics of our catalog now allows in-depth investigations of these correlations when binning in different quantities such as redshift or luminosity. However, we also point out that there are some apparent correlations which are likely due to selection effects or host contamination (such as the apparent anti-correlation between α_λ and $\log L_{5100}$).

Moreover, the spectral quality (mainly S/N) has important effects on the measured quantities and may bias the measurements at the low S/N end. Thus one must take these issues into account when using the catalog to study intrinsic correlations between various properties.

Fig. 13 shows the so-called 4DE1 projection in the H β FWHM versus $R_{\text{FeII}} = \text{EW}_{\text{FeII}4434-4684} / \text{EW}_{\text{H}\beta}$ space (e.g., Sulentic et al. 2000, 2002; Zamfir et al. 2009), which is an extension of the eigenvector space for quasar properties suggested by Boroson & Green (1992). Objects with H β FWHM $> 4000 \text{ km s}^{-1}$ (i.e., population ‘‘B’’ in the terminology of the 4DE1 parameter space of Sulentic and collaborators) have a tendency to have weaker relative iron emission strength for larger FWHMs. The black contours show the distribution of all quasars while the red contours show the distribution of radio-loud ($R > 10$) quasars. It appears that the radio-loud contours are more vertically elongated, broadly consistent with the phenomenological classification scheme based on the 4DE1 parameter space (e.g., Sulentic et al. 2000, 2002; Zamfir et al. 2009). The physics driving these characteristics in the parameter space is currently not clear, and deserves further study.

Fig. 14 shows the correlation between the [O III] $\lambda 5007$ luminosity and the continuum luminosity at 5100 Å. This correlation is usually used to estimate the bolometric luminosity using the [O III] $\lambda 5007$ luminosity as a surrogate for type 2 quasars (e.g. Kauffmann et al. 2003; Zakamska et al. 2003; Heckman et al. 2004; Reyes et al. 2008). While the correlation is apparent, it has a large scatter, as noted in earlier studies (e.g., Heckman et al. 2004; Reyes et al. 2008). The mean linear relation is:

$$\log L_{[\text{O III}]\lambda 5007} \approx \log L_{5100} - 2.5, \quad (2)$$

with a scatter ~ 0.35 dex.

4.2. Emission line shifts

Fig. 15 shows the distributions of velocity shifts between various emission lines. Recall that the velocity of the broad lines is measured from the peak of the multiple-Gaussian fit. The left panel of Fig. 15 shows the distributions of velocity shifts between the broad Balmer lines and the narrow lines. The means of these distributions are consistent with zero, hence there is no offset in the mean between the broad and narrow Balmer lines (cf., Bonning et al. 2007). We note that if we did not account for the blue wings of the narrow [O III] $\lambda\lambda 4959, 5007$ lines during spectral fitting, there would be a net redshift of the order of $\sim 100 \text{ km s}^{-1}$ between the broad H β line and [O III], which is inconsistent with the results for H α versus [S II]. The right panel of Fig. 15 shows the velocity offsets between MgII and [O III] and between CIV and MgII. The MgII line shows no mean offset from [O III], while the CIV line shows a systematic blueshift of $\sim 600 \text{ km s}^{-1}$ with respect to MgII (e.g., Gaskell 1982; Tytler & Fan 1992; Richards et al. 2002b).

It is interesting to note that for the broad H α /H β versus the narrow lines, many of the objects in the wings of the velocity offset distributions are either strong disk-emitters (e.g., Chen et al. 1989; Eracleous & Halpern 1994; Strateva et al. 2003), or have the broad component systematically offset from the narrow line center; in other cases the apparent large shifts were caused by poor fits to noisy spectra.

4.3. Virial BH masses

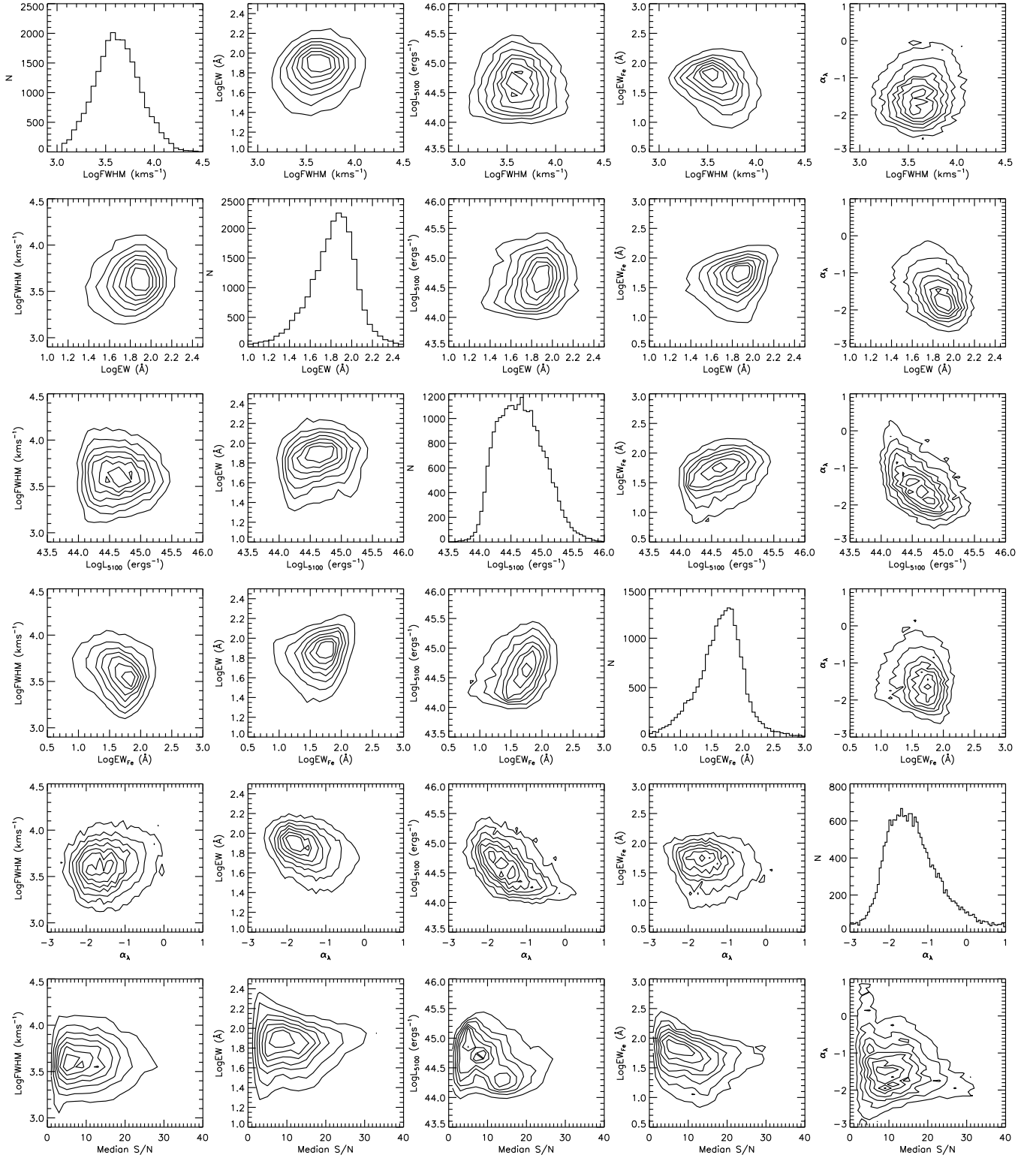


FIG. 10.— Statistical properties for H β based on our spectral measurements (for all quasars). The strong anti-correlation between the power-law continuum slope and luminosity reflects the increasing host galaxy contamination towards fainter quasar luminosities (see §3.6 and Fig. 8).

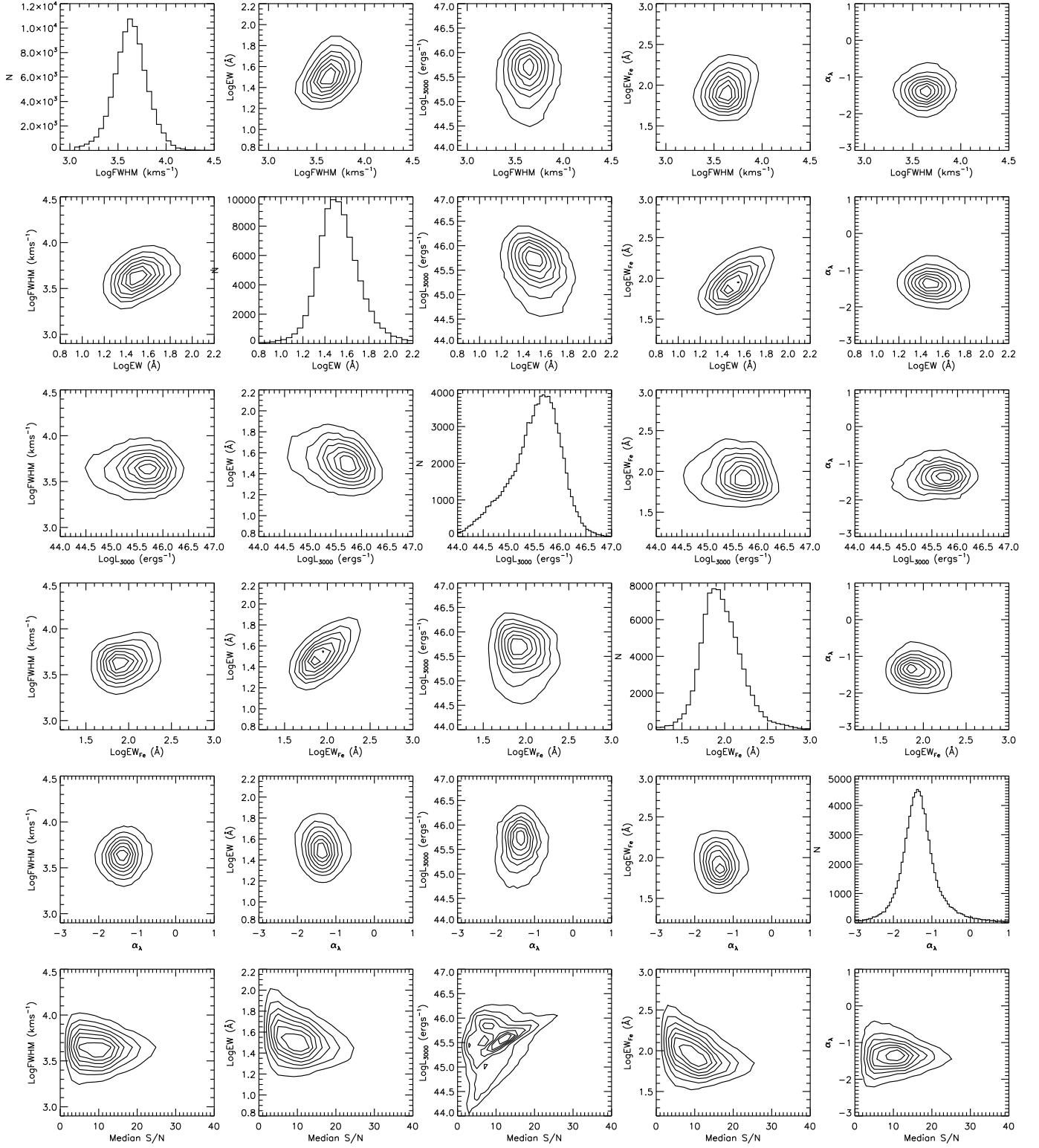


FIG. 11.— Statistical properties for MgII based on our spectral measurements (for all quasars). There are several known correlations, such as the MgII Baldwin effect (e.g., Baldwin 1977; Croom et al. 2002), and the correlation between FWHM and EW (e.g., Dong et al. 2009a).

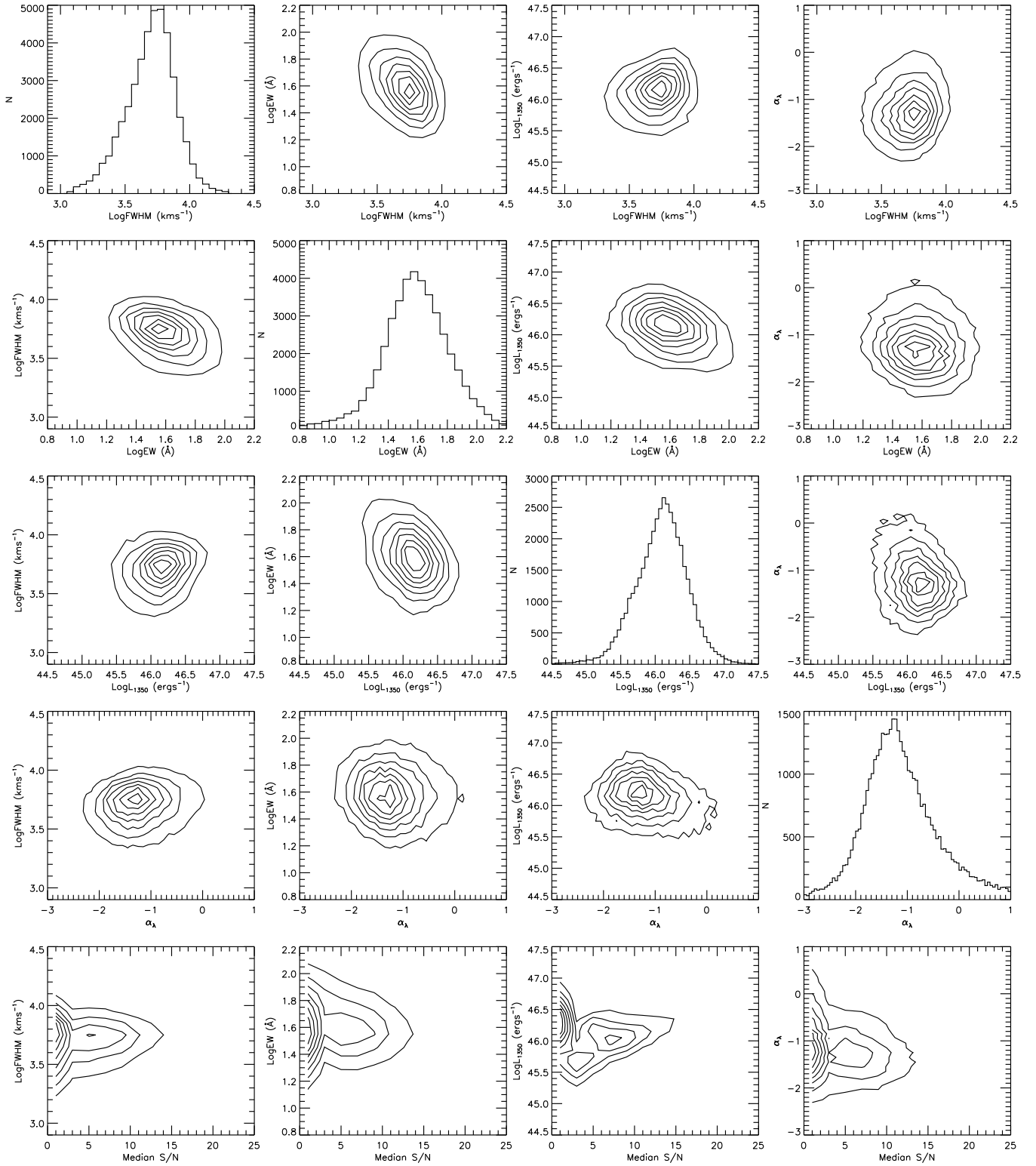


FIG. 12.— Statistical properties for CIV based on our spectral measurements (for all quasars). There are several correlations involving EW, FWHM and luminosity that may be different manifestations of the same phenomenon (e.g., Baldwin 1977; Richards et al. 2002b). The clustering of a population of low S/N objects is caused by the quasar target selection (see Fig. 1).

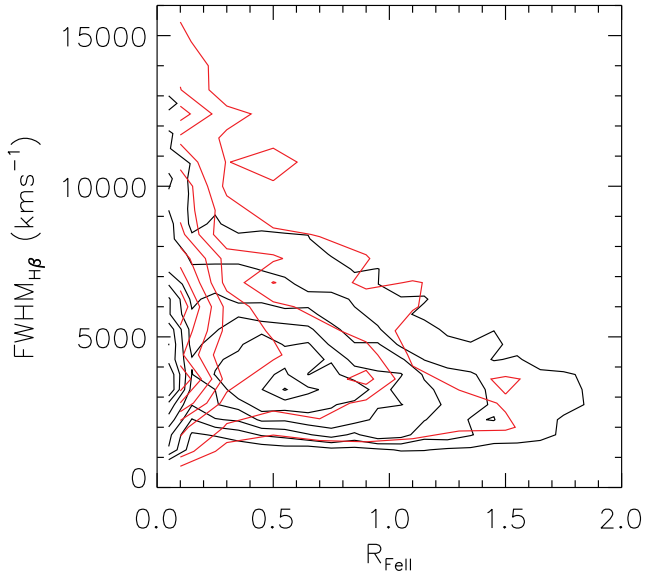


FIG. 13.— Distribution of quasars in the projected 4DE1 parameter space (e.g., Sulentic et al. 2000). Contours are local density contours. The black contours are for all quasars and the red contours are for radio-loud ($R > 10$) quasars only.

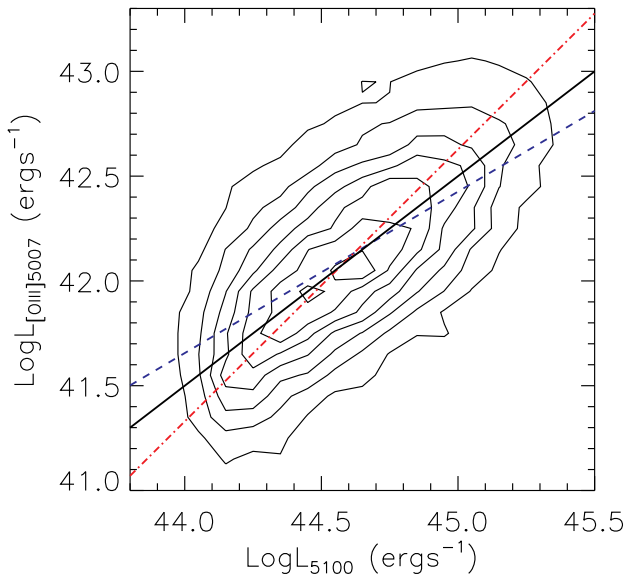


FIG. 14.— Correlation between $L_{[\text{OIII}]5007}$ and L_{5100} . The dashed line is the linear regression fit treating $\log L_{5100}$ as the independent variable, and the dash-dotted line is the bisector linear regression fit. The solid line is the mean linear relation described in Eqn. (2).

It has become common practice to estimate quasar/AGN BH masses based on single-epoch spectra (hereafter virial mass in short). This approach assumes that the broad line region (BLR) is virialized, the continuum luminosity¹⁵ is used as a proxy for the BLR radius, and the broad line width (FWHM or line dispersion) is used as a proxy for the virial

¹⁵ We note that in a few extremely radio-loud quasars, the continuum luminosity is significantly boosted by the optical emission from the jet, which will then lead to overestimation of the BLR size and the virial BH mass (e.g., Wu et al. 2004). The fraction of such objects in our sample is nevertheless tiny and hence we neglect this detail. But we caution the usage of cataloged virial BH masses for such individual objects.

velocity. The virial mass estimate can be expressed as:

$$\log \left(\frac{M_{\text{BH, vir}}}{M_{\odot}} \right) = a + b \log \left(\frac{\lambda L_{\lambda}}{10^{44} \text{ erg s}^{-1}} \right) + 2 \log \left(\frac{\text{FWHM}}{\text{km s}^{-1}} \right), \quad (3)$$

where the coefficients a and b are empirically calibrated against local AGNs with RM masses or internally among different lines. $\text{H}\beta$, MgII , CIV , and their corresponding continuum luminosities are all frequently adopted in such virial calibrations. Although it is straightforward to calibrate and use these virial estimators, one must bear in mind the large uncertainties ($\gtrsim 0.4$ dex) associated with these estimates and the systematics involved in the calibration and usage, which will potentially lead to significant biases of these BH mass estimates (e.g., Collin et al. 2006; Shen et al. 2008b; Marconi et al. 2008; Denney et al. 2009; Kelly et al. 2009; Shen & Kelly 2010).

The virial BH mass calibrations used in this paper are from McLure & Dunlop (2004, $\text{H}\beta$ and MgII), Vestergaard & Peterson (2006, $\text{H}\beta$ and CIV), and Vestergaard & Osmer (2009, MgII). These calibrations have parameters:

$$(a, b) = (0.672, 0.61), \quad \text{MD04; H}\beta \quad (4)$$

$$(a, b) = (0.505, 0.62), \quad \text{MD04; MgII} \quad (5)$$

$$(a, b) = (0.910, 0.50), \quad \text{VP06; H}\beta \quad (6)$$

$$(a, b) = (0.660, 0.53), \quad \text{VP06; CIV} \quad (7)$$

$$(a, b) = (0.860, 0.50), \quad \text{VO09; MgII} \quad (8)$$

In using these relations we choose the proper FWHM definition adopted in these calibrations. In order to utilize our new MgII FWHM measurements (e.g., multiple-Gaussian fits with narrow line subtraction, see §3.3), we adopt the same slope in the BLR radius–luminosity relation in McLure & Dunlop (2004), $b = 0.62$, and recalibrate the coefficient a such that the MgII -based estimates are consistent with the $\text{H}\beta$ -based (VP06) estimates on average. This new MgII calibration is

$$(a, b) = (0.740, 0.62), \quad \text{S10; MgII} \quad (9)$$

We do not utilize other independent calibrations in the literature (e.g., Greene & Ho 2005b; McGill et al. 2008; Wang et al. 2009b), but these alternative estimates can be directly computed using our reported measurements.

There are systematic differences among different versions of virial calibrations. For instance, the calibrations for $\text{H}\beta$ and MgII in McLure & Dunlop (2004) used the old RM masses and virial coefficient, while those in Vestergaard & Peterson (2006) and Vestergaard & Osmer (2009) used the updated RM masses and virial coefficient (Onken et al. 2004). Moreover, different versions of virial calibration for the same line have different dependence on luminosity, and they usually use different FWHM definitions (even though occasionally different approaches to measure the FWHM yield the same value during the multi-parameter fits). It is important to explore these systematics with RM AGN samples and statistical quasar samples to determine which is the best approach to estimate quasar BH masses with the virial technique, and this is work in progress (e.g., Onken & Kollmeier 2008; Denney et al. 2009; Wang et al. 2009b; Rafiee & Hall 2010). Here we simply settle on a fiducial virial mass estimate: we use $\text{H}\beta$ (VP06) estimates for $z < 0.7$, MgII (S10) estimates for $0.7 \leq z < 1.9$ and CIV (VP06) estimates for $z \geq 1.9$. Fig. 16 shows the comparison between these virial estimates between two lines for the subset of quasars for which both line estimates are available and the median line S/N > 6. There is

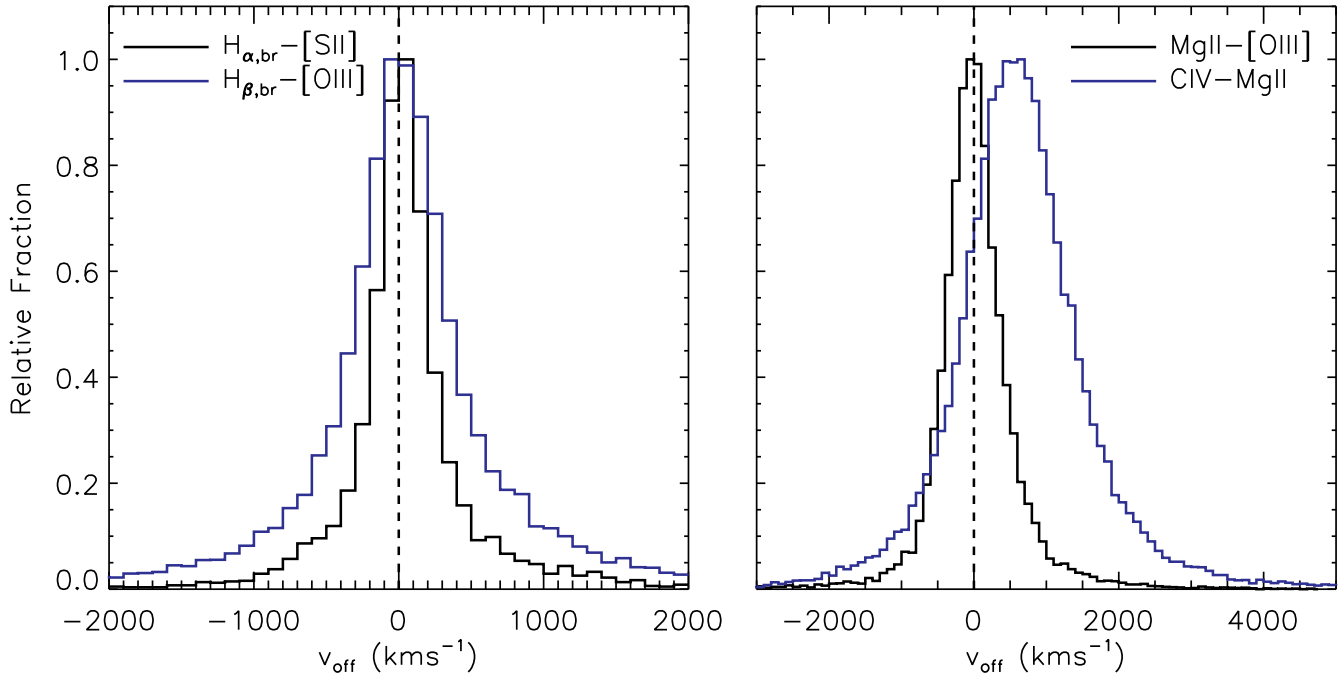


FIG. 15.— Velocity shifts between different pairs of lines. Positive values indicate blueshifts.

negligible mean offset (< 0.01 dex) between these virial estimates, which motivated our choice of these three calibrations. However, as noted in Shen et al. (2008b), there is a strong trend of decreasing the ratio of $\log(M_{\text{BH}}^{\text{MgII}}/M_{\text{BH}}^{\text{CIV}})$ with increasing CIV-MgII blueshifts, indicating a possible non-virialized component in CIV.

5. SUMMARY

We have constructed a value-added DR7 quasar catalog with various properties. This catalog can be used to study correlations among properties of optically selected quasars, and the active black hole mass function in quasars (Shen et al., in preparation). We performed various tests and found that our automatic fitting procedure to emission lines performed reasonably well. Of course, for some particular purposes, more sophisticated measurements might be needed if the S/N allows. Moreover, as we have mentioned earlier, one must take into account the possible effects of selection and S/N, as well as systematics involved in converting the measured quantities to derived quantities, upon usage of these measurements to study quasar properties.

Finally, we make this catalog publicly available online¹⁶, where we also provide supplemental materials (such as dereddened spectra, quality assessment fitting plots, etc) and future updates of this compilation.

¹⁶ http://www.cfa.harvard.edu/~yshen/BH_mass/dr7.htm

Funding for the SDSS and SDSS-II has been provided by the Alfred P. Sloan Foundation, the Participating Institutions, the National Science Foundation, the U.S. Department of Energy, the National Aeronautics and Space Administration, the Japanese Monbukagakusho, the Max Planck Society, and the Higher Education Funding Council for England. The SDSS Web Site is <http://www.sdss.org/>.

The SDSS is managed by the Astrophysical Research Consortium for the Participating Institutions. The Participating Institutions are the American Museum of Natural History, Astrophysical Institute Potsdam, University of Basel, University of Cambridge, Case Western Reserve University, University of Chicago, Drexel University, Fermilab, the Institute for Advanced Study, the Japan Participation Group, Johns Hopkins University, the Joint Institute for Nuclear Astrophysics, the Kavli Institute for Particle Astrophysics and Cosmology, the Korean Scientist Group, the Chinese Academy of Sciences (LAMOST), Los Alamos National Laboratory, the Max-Planck-Institute for Astronomy (MPIA), the Max-Planck-Institute for Astrophysics (MPA), New Mexico State University, Ohio State University, University of Pittsburgh, University of Portsmouth, Princeton University, the United States Naval Observatory, and the University of Washington.

Facilities: Sloan

REFERENCES

- Abazajian, K. N., et al. 2009, *ApJS*, 182, 543
 Adelman-McCarthy, J. K., et al. 2008, *ApJS*, 175, 297
 Bachev, R., Marziani, P., Sulentic, J. W., Zamanov, R., Calvani, M., & Dultzin-Hacyan, D. 2004, *ApJ*, 617, 171
 Baldwin, J. A. 1977, *ApJ*, 214, 679
 Baskin, A., & Laor, A. 2005, *MNRAS*, 356, 1029
 Blanton, M. R., Lin, H., Lupton, R. H., Maley, F. M., Young, N., Zehavi, I., & Loveday, J. 2003, *AJ*, 125, 2276
 Bonning, E. W., Shields, G. A., & Salvander, S. 2007, *ApJ*, 666, L13
 Boroson, T. A., & Green, R. F. 1992, *ApJS*, 80, 109
 Cardelli, J. A., Clayton, G. C., & Mathis, J. S. 1989, *ApJ*, 345, 245
 Chen, K., Halpern, J. P., & Filippenko, A. V. 1989, *ApJ*, 339, 742
 Collin, S., Kawaguchi, T., Peterson, B. M., & Vestergaard, M. 2006, *A&A*, 456, 75
 Croom, S. M., et al. 2002, *MNRAS*, 337, 275
 Croom, S. M., Smith, R. J., Boyle, B. J., Shanks, T., Miller, L., Outram, P. J., & Loaring, N. S. 2004, *MNRAS*, 349, 1397
 Denney, K. D., et al. 2009, *ApJ*, 704, L80
 Dietrich, M., & Hamann, F. 2004, *ApJ*, 611, 761

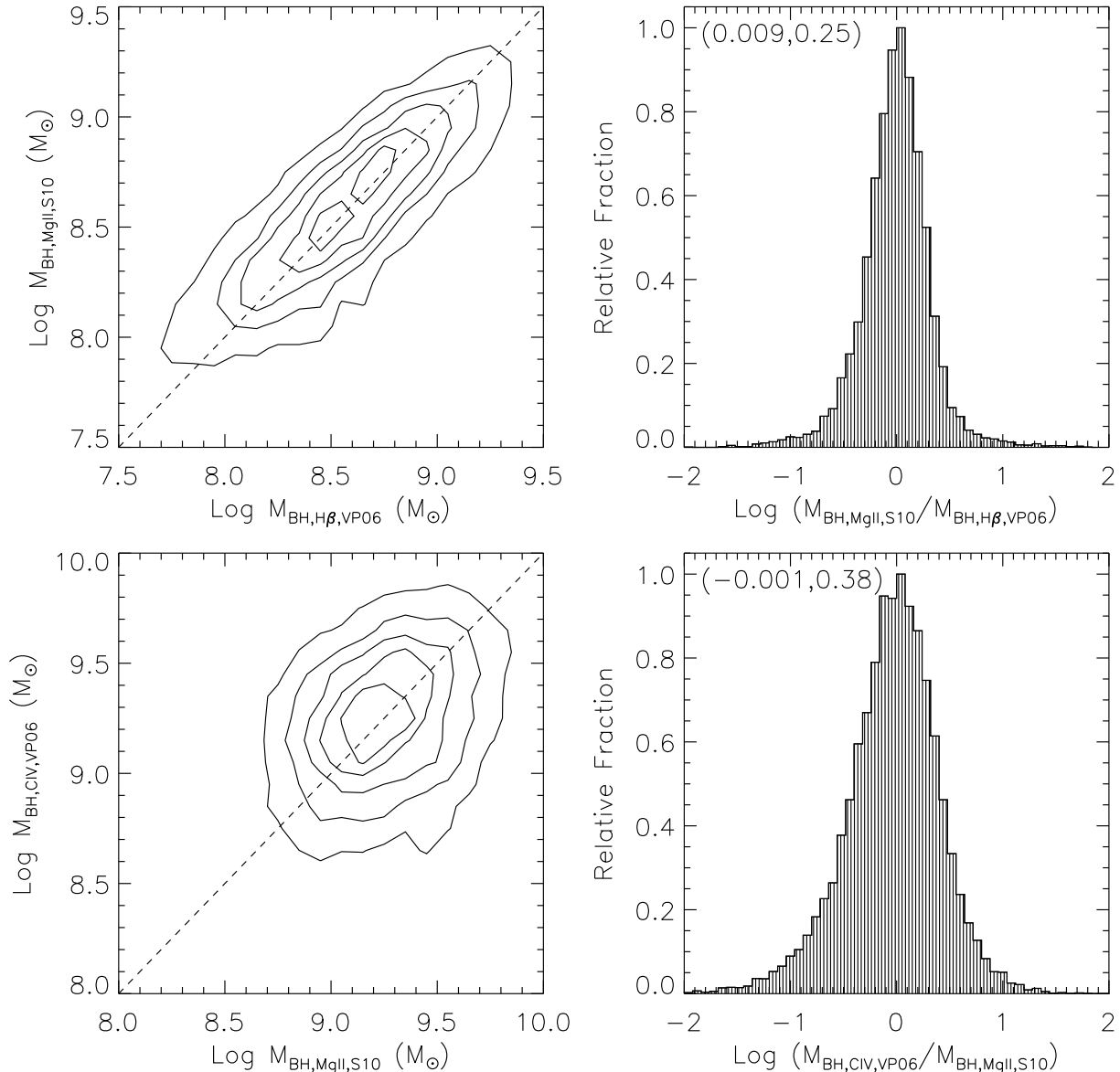


FIG. 16.— Comparison of virial masses between two different line estimators for the subset of quasars in our sample for which both line estimates are available and the median line S/N per pixel > 6 . The left panels are one-to-one plots, where the contours are local point density contours. The right panels show the distribution of mass ratios between two lines, and the mean and 1σ from a Gaussian fit to the distribution are indicated in the top-left corner.

Dong, X., Wang, J., Wang, T., Wang, H., Fan, X., Zhou, H., & Yuan, W. 2009a, ArXiv e-prints
 Dong, X., Wang, T., Wang, J., Fan, X., Wang, H., Zhou, H., & Yuan, W. 2009b, ApJ, 703, L1
 Eracleous, M., & Halpern, J. P. 1994, ApJS, 90, 1
 Fine, S., et al. 2008, MNRAS, 390, 1413
 —. 2006, MNRAS, 373, 613
 Fukugita, M., Ichikawa, T., Gunn, J. E., Doi, M., Shimasaku, K., & Schneider, D. P. 1996, AJ, 111, 1748
 Gaskell, C. M. 1982, ApJ, 263, 79
 Gibson, R. R., et al. 2009, ApJ, 692, 758
 Greene, J. E., & Ho, L. C. 2005a, ApJ, 627, 721
 —. 2005b, ApJ, 630, 122
 Gunn, J. E., et al. 1998, AJ, 116, 3040
 —. 2006, AJ, 131, 2332
 Hao, L., et al. 2005, AJ, 129, 1783
 Heckman, T. M., Miley, G. K., van Breugel, W. J. M., & Butcher, H. R. 1981, ApJ, 247, 403
 Heckman, T. M., Kauffmann, G., Brinchmann, J., Charlot, S., Tremonti, C., & White, S. D. M. 2004, ApJ, 613, 109
 Hewett, P. C. & Wild, V. 2010, MNRAS, in press, arXiv:1003.3017
 Hogg, D. W., Finkbeiner, D. P., Schlegel, D. J., & Gunn, J. E. 2001, AJ, 122, 2129

Hopkins, P. F., Hernquist, L., Cox, T. J., Di Matteo, T., Robertson, B., & Springel, V. 2006, ApJS, 163, 1
 Hopkins, P. F., Hernquist, L., Cox, T. J., & Kereš, D. 2008, ApJS, 175, 356
 Hu, C., Wang, J., Ho, L. C., Chen, Y., Bian, W., & Xue, S. 2008a, ApJ, 683, L115
 Hu, C., Wang, J., Ho, L. C., Chen, Y., Zhang, H., Bian, W., & Xue, S. 2008b, ApJ, 687, 78
 Ivezić, Ž., et al. 2004, Astronomische Nachrichten, 325, 583
 Jiang, L., Fan, X., Ivezić, Ž., Richards, G. T., Schneider, D. P., Strauss, M. A., & Kelly, B. C. 2007, ApJ, 656, 680
 Kauffmann, G., & Haehnelt, M. 2000, MNRAS, 311, 576
 Kauffmann, G., et al. 2003, MNRAS, 341, 33
 Kelly, B. C., Vestergaard, M., & Fan, X. 2009, ApJ, 692, 1388
 Kollmeier, J. A., et al. 2006, ApJ, 648, 128
 Komossa, S., Xu, D., Zhou, H., Storchi-Bergmann, T., & Binette, L. 2008, ApJ, 680, 926
 Liu, X., Shen, Y., Strauss, M. A., & Greene, J. E. 2010, ApJ, 708, 427
 Lupton, R., Gunn, J. E., Ivezić, Z., Knapp, G. R., & Kent, S. 2001, in Astronomical Society of the Pacific Conference Series, Vol. 238, Astronomical Data Analysis Software and Systems X, ed. F. R. Harnden, Jr., F. A. Primini, & H. E. Payne, 269
 Marconi, A., Axon, D. J., Maiolino, R., Nagao, T., Pastorini, G., Pietrini, P., Robinson, A., & Torricelli, G. 2008, ApJ, 678, 693

- Marconi, A., Risaliti, G., Gilli, R., Hunt, L. K., Maiolino, R., & Salvati, M. 2004, MNRAS, 351, 169
- Marziani, P., Sulentic, J. W., Dultzin-Hacyan, D., Calvani, M., & Moles, M. 1996, ApJS, 104, 37
- McGill, K. L., Woo, J., Treu, T., & Malkan, M. A. 2008, ApJ, 673, 703
- McLure, R. J., & Dunlop, J. S. 2004, MNRAS, 352, 1390 (MD04)
- McLure, R. J., & Jarvis, M. J. 2002, MNRAS, 337, 109
- Onken, C. A., Ferrarese, L., Merritt, D., Peterson, B. M., Pogge, R. W., Vestergaard, M., & Wandel, A. 2004, ApJ, 615, 645
- Onken, C. A., & Kollmeier, J. A. 2008, ApJ, 689, L13
- Pier, J. R., Munn, J. A., Hindsley, R. B., Hennessy, G. S., Kent, S. M., Lupton, R. H., & Ivezić, Ž. 2003, AJ, 125, 1559
- Rafiee, A., & Hall, P. B. 2010, ApJS, submitted
- Reyes, R., et al. 2008, AJ, 136, 2373
- Richards, G. T., et al. 2002a, AJ, 123, 2945
- 2006a, ApJS, 166, 470
- 2006b, AJ, 131, 2766
- Richards, G. T., Vanden Berk, D. E., Reichard, T. A., Hall, P. B., Schneider, D. P., SubbaRao, M., Thakar, A. R., & York, D. G. 2002b, AJ, 124, 1
- Salviander, S., Shields, G. A., Gebhardt, K., & Bonning, E. W. 2007, ApJ, 662, 131
- Schlegel, D. J., Finkbeiner, D. P., & Davis, M. 1998, ApJ, 500, 525
- Schneider, D. P., et al. 2007, AJ, 134, 102
- 2010, AJ, 139, 2360
- Shankar, F., Weinberg, D. H., & Miralda-Escudé, J. 2009, ApJ, 690, 20
- Shen, J., Vanden Berk, D. E., Schneider, D. P., & Hall, P. B. 2008a, AJ, 135, 928
- Shen, Y. 2009, ApJ, 704, 89
- Shen, Y., Greene, J. E., Strauss, M. A., Richards, G. T., & Schneider, D. P. 2008b, ApJ, 680, 169
- Shen, Y., & Kelly, B. C. 2010, ApJ, 713, 41
- Shen, Y., et al. 2007, AJ, 133, 2222
- Smith, J. A., et al. 2002, AJ, 123, 2121
- Smith, K. L., Shields, G. A., Bonning, E. W., McMullen, C. C., & Salviander, S. 2009, arXiv:0908.1998
- Stoughton, C., et al. 2002, AJ, 123, 485
- Strateva, I. V., et al. 2003, AJ, 126, 1720
- Sulentic, J. W., Bachev, R., Marziani, P., Negrete, C. A., & Dultzin, D. 2007, ApJ, 666, 757
- Sulentic, J. W., Marziani, P., Zamanov, R., Bachev, R., Calvani, M., & Dultzin-Hacyan, D. 2002, ApJ, 566, L71
- Sulentic, J. W., Zwitter, T., Marziani, P., & Dultzin-Hacyan, D. 2000, ApJ, 536, L5
- Tucker, D. L., et al. 2006, Astronomische Nachrichten, 327, 821
- Tytler, D., & Fan, X. 1992, ApJS, 79, 1
- van der Marel, R. P., & Franx, M. 1993, ApJ, 407, 525
- Vanden Berk, D. E., et al. 2001, AJ, 122, 549
- Vestergaard, M. 2002, ApJ, 571, 733
- Vestergaard, M., & Osmer, P. S. 2009, ApJ, 699, 800 (VO09)
- Vestergaard, M., & Peterson, B. M. 2006, ApJ, 641, 689 (VP06)
- Vestergaard, M., & Wilkes, B. J. 2001, ApJS, 134, 1
- Wang, J., Chen, Y., Hu, C., Mao, W., Zhang, S., & Bian, W. 2009a, ApJ, 705, L76
- Wang, J., et al. 2009b, ApJ, 707, 1334
- White, R. L., Becker, R. H., Helfand, D. J., & Gregg, M. D. 1997, ApJ, 475, 479
- Wu, X.-B., Wang, R., Kong, M. Z., Liu, F. K., & Han, J. L. 2004, A&A, 424, 793
- Wu, J., Vanden Berk, D. E., Brandt, W. N., Schneider, D. P., Gibson, R. R., & Wu, J. 2009, ApJ, 702, 767
- Wyithe, J. S. B., & Loeb, A. 2003, ApJ, 595, 614
- York, D. G., et al. 2000, AJ, 120, 1579
- Zakamska, N. L., et al. 2003, AJ, 126, 2125
- Zamfir, S., Sulentic, J. W., Marziani, P., & Dultzin, D. 2009, ArXiv e-prints

TABLE 1 FITS CATALOG FORMAT

Column	Format	Description
1.....	STRING	SDSS DR7 designation hhmmss.ss+ddmmss.s (J2000.0)
2.....	DOUBLE	Right ascension in decimal degrees (J2000.0)
3.....	DOUBLE	Declination in decimal degrees (J2000.0)
4.....	DOUBLE	Redshift
5.....	LONG	Spectroscopic plate number
6.....	LONG	Spectroscopic fiber number
7.....	LONG	MJD of spectroscopic observation
8.....	LONG	Target selection flag (TARGET version)
9.....	LONG	Number of spectroscopic observations
10.....	LONG	Uniform selection flag
11.....	DOUBLE	$M_i(z=2)$ [$h = 0.7, \Omega_0 = 0.3, \Omega_\Lambda = 0.7, K$ -corrected to $z = 2$, following Richards et al. (2006b)]
12.....	DOUBLE	Bolometric luminosity [$\log(L_{\text{bol}}/\text{ergs}^{-1})$]
13.....	DOUBLE	Uncertainty in $\log L_{\text{bol}}$
14.....	LONG	BAL flag (0=nonBALQSO;1=CIV BALQSO;2=MgII BALQSO;3=both 1 and 2)
15.....	LONG	FIRST radio flag (-1=not in FIRST footprint; 0=FIRST undetected; 1=core-dominant; 2=lobe-dominant)
16.....	DOUBLE	Observed radio flux density at rest-frame 6 cm $f_{\nu,6\text{cm}}$ [mJy]
17.....	DOUBLE	Observed optical flux density at rest-frame 2500Å [$\log(f_{\nu,2500}/\text{ergs}^{-1}\text{cm}^{-2}\text{Hz}^{-1})$]
18.....	DOUBLE	Radio loudness $R \equiv f_{\nu,6\text{cm}}/f_{\nu,2500}$
19.....	DOUBLE	Monochromatic luminosity at 5100Å [$\log(L_{5100}/\text{ergs}^{-1})$]
20.....	DOUBLE	Uncertainty in $\log L_{5100}$
21.....	DOUBLE	Monochromatic luminosity at 3000Å [$\log(L_{3000}/\text{ergs}^{-1})$]
22.....	DOUBLE	Uncertainty in $\log L_{3000}$
23.....	DOUBLE	Monochromatic luminosity at 1350Å [$\log(L_{1350}/\text{ergs}^{-1})$]
24.....	DOUBLE	Uncertainty in $\log L_{1350}$
25.....	DOUBLE	Line luminosity of broad H α [$\log(L/\text{ergs}^{-1})$]
26.....	DOUBLE	Uncertainty in $\log L_{\text{H}\alpha,\text{broad}}$
27.....	DOUBLE	FWHM of broad H α (kms $^{-1}$)
28.....	DOUBLE	Uncertainty in the broad H α FWHM
29.....	DOUBLE	Restframe equivalent width of broad H α (Å)
30.....	DOUBLE	Uncertainty in $\text{EW}_{\text{H}\alpha,\text{broad}}$
31.....	DOUBLE	Line luminosity of narrow H α [$\log(L/\text{ergs}^{-1})$]
32.....	DOUBLE	Uncertainty in $\log L_{\text{H}\alpha,\text{narrow}}$
33.....	DOUBLE	FWHM of narrow H α (kms $^{-1}$)
34.....	DOUBLE	Uncertainty in the narrow H α FWHM
35.....	DOUBLE	Restframe equivalent width of narrow H α (Å)
36.....	DOUBLE	Uncertainty in $\text{EW}_{\text{H}\alpha,\text{narrow}}$
37.....	DOUBLE	Line luminosity of [N II] $\lambda 6584$ [$\log(L/\text{ergs}^{-1})$]
38.....	DOUBLE	Uncertainty in $\log L_{[\text{NII}]\lambda 6584}$
39.....	DOUBLE	Restframe equivalent width of [N II] $\lambda 6584$ (Å)

Continued on Next Page...

TABLE 1 – Continued

Column	Format	Description
40.....	DOUBLE	Uncertainty in $EW_{[NII]6584}$
41.....	DOUBLE	Line luminosity of [S II] $\lambda 6717$ [$\log(L/\text{ergs}^{-1})$]
42.....	DOUBLE	Uncertainty in $\log L_{[SII]6717}$
43.....	DOUBLE	Restframe equivalent width of [S II] $\lambda 6717$ (\AA)
44.....	DOUBLE	Uncertainty in $EW_{[SII]6717}$
45.....	DOUBLE	Line luminosity of [S II] $\lambda 6731$ [$\log(L/\text{ergs}^{-1})$]
46.....	DOUBLE	Uncertainty in $\log L_{[SII]6731}$
47.....	DOUBLE	Restframe equivalent width of [S II] $\lambda 6731$ (\AA)
48.....	DOUBLE	Uncertainty in $EW_{[SII]6731}$
49.....	DOUBLE	Restframe equivalent width of Fe within 6000-6500 \AA (\AA)
50.....	DOUBLE	Uncertainty in $EW_{Fe,H\alpha}$
51.....	DOUBLE	Power-law slope for the continuum fit for $H\alpha$
52.....	DOUBLE	Uncertainty in $\alpha_{H\alpha}$
53.....	LONG	Number of good pixels for the restframe 6400-6765 \AA region
54.....	DOUBLE	Median S/N per pixel for the restframe 6400-6765 \AA region
55.....	DOUBLE	Reduced χ^2 for the $H\alpha$ line fit; -1 if not fitted
56.....	DOUBLE	Line luminosity of broad $H\beta$ [$\log(L/\text{ergs}^{-1})$]
57.....	DOUBLE	Uncertainty in $\log L_{H\beta,broad}$
58.....	DOUBLE	FWHM of broad $H\beta$ (kms^{-1})
59.....	DOUBLE	Uncertainty in the broad $H\beta$ FWHM
60.....	DOUBLE	Restframe equivalent width of broad $H\beta$ (\AA)
61.....	DOUBLE	Uncertainty in $EW_{H\beta,broad}$
62.....	DOUBLE	Line luminosity of narrow $H\beta$ [$\log(L/\text{ergs}^{-1})$]
63.....	DOUBLE	Uncertainty in $\log L_{H\beta,narrow}$
64.....	DOUBLE	FWHM of narrow $H\beta$ (kms^{-1})
65.....	DOUBLE	Uncertainty in the narrow $H\beta$ FWHM
66.....	DOUBLE	Restframe equivalent width of narrow $H\beta$ (\AA)
67.....	DOUBLE	Uncertainty in $EW_{H\beta,narrow}$
68.....	DOUBLE	FWHM of broad $H\beta$ using a single Gaussian fit (kms^{-1})
69.....	DOUBLE	Line luminosity of [O III] $\lambda 4959$ [$\log(L/\text{ergs}^{-1})$]
70.....	DOUBLE	Uncertainty in $\log L_{[OIII]4959}$
71.....	DOUBLE	Restframe equivalent width of [O III] $\lambda 4959$ (\AA)
72.....	DOUBLE	Uncertainty in $EW_{[OIII]4959}$
73.....	DOUBLE	Line luminosity of [O III] $\lambda 5007$ [$\log(L/\text{ergs}^{-1})$]
74.....	DOUBLE	Uncertainty in $\log L_{[OIII]5007}$
75.....	DOUBLE	Restframe equivalent width of [O III] $\lambda 5007$ (\AA)
76.....	DOUBLE	Uncertainty in $EW_{[OIII]5007}$
77.....	DOUBLE	Restframe equivalent width of Fe within 4435-4685 \AA (\AA)
78.....	DOUBLE	Uncertainty in $EW_{Fe,H\beta}$
79.....	DOUBLE	Power-law slope for the continuum fit for $H\beta$
80.....	DOUBLE	Uncertainty in $\alpha_{H\beta}$
81.....	LONG	Number of good pixels for the restframe 4750-4950 \AA region
22.....	DOUBLE	Median S/N per pixel for the restframe 4750-4950 \AA region
33.....	DOUBLE	Reduced χ^2 for the $H\beta$ line fit; -1 if not fitted
84.....	DOUBLE	Line luminosity of the whole MgII [$\log(L/\text{ergs}^{-1})$]
85.....	DOUBLE	Uncertainty in $\log L_{MgII,whole}$
86.....	DOUBLE	FWHM of the whole MgII (kms^{-1})
87.....	DOUBLE	Uncertainty in the whole MgII FWHM
88.....	DOUBLE	Restframe equivalent width of the whole MgII (\AA)
89.....	DOUBLE	Uncertainty in $EW_{MgII,whole}$
90.....	DOUBLE	Line luminosity of broad MgII [$\log(L/\text{ergs}^{-1})$]
91.....	DOUBLE	Uncertainty in $\log L_{MgII,broad}$
92.....	DOUBLE	FWHM of broad MgII (kms^{-1})
93.....	DOUBLE	Uncertainty in the broad MgII FWHM
94.....	DOUBLE	Restframe equivalent width of broad MgII (\AA)
95.....	DOUBLE	Uncertainty in $EW_{MgII,broad}$
96.....	DOUBLE	FWHM of broad MgII using a single Gaussian fit (kms^{-1})
97.....	DOUBLE	Restframe equivalent width of Fe within 2200-3090 \AA (\AA)
98.....	DOUBLE	Uncertainty in $EW_{Fe,MgII}$
99.....	DOUBLE	Power-law slope for the continuum fit for MgII
100.....	DOUBLE	Uncertainty in α_{MgII}
101....	LONG	Number of good pixels for the restframe 2700-2900 \AA region
102....	DOUBLE	Median S/N per pixel for the restframe 2700-2900 \AA region
103....	DOUBLE	Reduced χ^2 for the MgII line fit; -1 if not fitted
104....	DOUBLE	Line luminosity of the whole CIV [$\log(L/\text{ergs}^{-1})$]
105....	DOUBLE	Uncertainty in $\log L_{CIV}$
106....	DOUBLE	FWHM of the whole CIV (kms^{-1})
107....	DOUBLE	Uncertainty in the CIV FWHM
108....	DOUBLE	Restframe equivalent width of the whole CIV (\AA)
109....	DOUBLE	Uncertainty in EW_{CIV}
110....	DOUBLE	Power-law slope for the continuum fit for CIV
111....	DOUBLE	Uncertainty in α_{CIV}

Continued on Next Page...

TABLE 1 – Continued

Column	Format	Description
112....	LONG	Number of good pixels for the restframe 1500-1600Å region
113....	DOUBLE	Median S/N per pixel for the restframe 1500-1600Å region
114....	DOUBLE	Reduced χ^2 for the CIV fit; -1 if not fitted
115....	DOUBLE	Velocity shift of broad H α (kms $^{-1}$)
116....	DOUBLE	Uncertainty in $V_{H\alpha,broad}$
117....	DOUBLE	Velocity shift of narrow H α (kms $^{-1}$)
118....	DOUBLE	Uncertainty in $V_{H\alpha,narrow}$
119....	DOUBLE	Velocity shift of broad H β (kms $^{-1}$)
120....	DOUBLE	Uncertainty in $V_{H\beta,broad}$
121....	DOUBLE	Velocity shift of narrow H β (kms $^{-1}$)
122....	DOUBLE	Uncertainty in $V_{H\beta,narrow}$
123....	DOUBLE	Velocity shift of broad MgII (kms $^{-1}$)
124....	DOUBLE	Uncertainty in $V_{MgII,broad}$
125....	DOUBLE	Velocity shift of CIV (kms $^{-1}$)
126....	DOUBLE	Uncertainty in V_{CIV}
127....	DOUBLE	Virial BH mass based on H β [MD04, $\log(M_{BH,vir}/M_{\odot})$]
128....	DOUBLE	Measurement uncertainty in $\log M_{BH,vir}$ (H β , MD04)
129....	DOUBLE	Virial BH mass based on H β [VP06, $\log(M_{BH,vir}/M_{\odot})$]
130....	DOUBLE	Measurement uncertainty in $\log M_{BH,vir}$ (H β , VP06)
131....	DOUBLE	Virial BH mass based on MgII [MD04, $\log(M_{BH,vir}/M_{\odot})$]
132....	DOUBLE	Measurement uncertainty in $\log M_{BH,vir}$ (MgII, MD04)
133....	DOUBLE	Virial BH mass based on MgII [VO09, $\log(M_{BH,vir}/M_{\odot})$]
134....	DOUBLE	Measurement uncertainty in $\log M_{BH,vir}$ (MgII, VO09)
135....	DOUBLE	Virial BH mass based on MgII [S10, $\log(M_{BH,vir}/M_{\odot})$]
136....	DOUBLE	Measurement uncertainty in $\log M_{BH,vir}$ (MgII, S10)
137....	DOUBLE	Virial BH mass based on CIV [VP06, $\log(M_{BH,vir}/M_{\odot})$]
138....	DOUBLE	Measurement uncertainty in $\log M_{BH,vir}$ (CIV, VP06)
139....	DOUBLE	The adopted fiducial virial BH mass [$\log(M_{BH,vir}/M_{\odot})$]
140....	DOUBLE	Uncertainty in the fiducial virial BH mass (measurement uncertainty only)
141....	DOUBLE	Eddington ratio based on the fiducial virial BH mass [$\log(L_{bol}/L_{Edd})$]
142....	LONG	Special interest flag

NOTE. — (1) Objects are in the same order as in the DR7 quasar catalog (Schneider et al. 2010); (2) K -corrections are the same as in Richards et al. (2006b); (3) Bolometric luminosities computed using bolometric corrections in Richards et al. (2006a) using one of the 5100Å, 3000Å, or 1350Å monochromatic luminosities depending on redshift; (4) Uncertainties are measurement errors only.